Hydrodynamical Modeling of Ultra-Relativistic Au+Au Collisions at RHIC Energies with Longitudinal Fluctuating Initial Conditions

Khadija El Berhoumi

Physics Department
Master of Science

McGill University, Montreal

December 3, 2014

A thesis submitted to McGill University in partial fulfillment of the requirements for the degree of Master of Science.

Dedicated to Gaza.

Acknowledgments

I am grateful to my supervisor, Professor Sangyong Jeon, for his support and continued advice during my masters studies. Also, I would like to thank Professor Charles Gale for his guidance and help. I am grateful to the McGill Theoretical Nuclear Physics group for the useful discussions. A special thank you to Gabriel Denicol for his close guidance of many parts of this work and to Jean-Francois Paquet for informative discussions on MUSIC and his valuable input.

Computations were performed on the Guillimin supercomputer at McGill University under the auspices of Calcul Québec and Compute Canada. I would also like to thank the Guillimin staff and Mr. Paul Mercure for their technical support and NSERC for their funding of this project.

Last but not least, I would like to thank my family and husband for their love and support in everything I do.

Abstract

We present the study of a hydrodynamical evolution of ultra-relativistic Au+Au collisions at RHIC energy with initial profile taken from the AMPT (a Multi-Phase Transport) model. The purpose of this work is to study the absence and presence of longitudinal fluctuations, fluctuating initial local flow velocities as well as study the viscous effects of fixed $\eta/s = 1/4\pi$ on the system. These collisions, carried out at $\sqrt{s_{\rm NN}} = 200$ GeV, are studied for spectra, anisotropic flow (v_2, v_3, and v_4), and mean-p_T. The goal of this work is to study longitudinal behavior since previous works have mostly focused on transverse fluctuations. A description of AMPT and MUScl for Ion Collisions (MUSIC) models are provided followed by results and a discussion of the results. The results show significant differences in results for each set of initial conditions and viscous settings and sets ground for future studies on the AMPT initial conditions and hydrodynamical evolution of heavy ions. Comparisons to data are made where available.

Résumé

À l'aide du modèle d'évolution hydrodynamique MUSIC ("MUScl for Ion Collisions") et de conditions initiales provenant du modèle AMPT ("A Multi-Phase Transport model"), nous présentons une étude des collisions relativistes Au+Au à des énergies de $\sqrt{s_{NN}} =$ 200 GeV, telles qu'étudiées au "Relativistic Heavy Ion Collider" (RHIC). L'objectif de ce travail est l'étude de l'effet des fluctuations longitudinales des conditions initiales du modèle hydrodynamique, ainsi que l'étude de l'effet de la présence ou non de viscosité de cisaillement dans l'évolution hydrodynamique. Les observables étudiées sont le spectre, les coefficients d'anisotropie azimutale (v_2, v_3 et v_4) ainsi que le p_T-moyen.

Une description d'AMPT et de MUSIC est donnée, suivie de la présentation et discussion des résultats. Ceux-ci sont comparés aux données du RHIC lorsque possible. Les résultats indiquent un effet considérable des fluctuations longitudinales des conditions initiales, ainsi que de la viscosité, et prépare le terrain pour des études futures de l'effet des fluctuations longitudinales dans les simulations hydrodynamiques de collisions d'ions lourds.

Contents

List of Figures

List of Tables

Chapter 1

Introduction

When two heavy nuclei collide at ultra-relativistic energies, thousands of particles are created generating a dense medium of particles [1]. Ultra-relativistic heavy-ion collisions produce a new phase of strongly interacting matter due to extreme conditions of density and temperature [2]. This is the Quark Gluon Plasma (QGP) which is a deconfined phase of nuclear matter composed of quarks and gluons. This matter is the result of the deconfinement of partons (quarks and gluons) which occurs at temperatures above $T_{\rm cr} \approx 175$ MeV and energy densities above $\simeq 1$ GeV/fm^3 [3, 4]. The experiments at the Relativistic Heavy Ion Collider (RHIC) at Brookhaven National Laboratory and The Large Hadron Collider (LHC) are capable of colliding heavy ions at high enough energies to produce QGP. The ability to produce QGP in the laboratory is an accomplishment which has never been achieved before these experiments. QGP is an important state of matter because it is believed to have been the state of the early universe a few milliseconds after the Big Bang and possibly exists in the core of heavy neutron stars.

In this thesis, we would like to investigate the properties of QGP using a hydrodynamical evolution of the matter until it is cool enough to coalesce into color-neutral particles (hadrons). Hadrons are strongly interacting particles made of quarks and "glued" together by gluons. This study will use initial conditions from A Multiphase Transport model (AMPT)

[5, 6, 7, 8]. These initial conditions will be used as input to the hydrodynamical evolution of matter using the MUScl for Ion Collisions (MUSIC) model— where MUScl stands for Monotone Upstream-centered Schemes for Conservation Laws [9, 10, 11, 12, 13, 14, 15]. A system which follows a hydrodynamical evolution is assumed to evolve like a fluid. MUSIC is an advanced hydrodynamical model which implements the Kurganov-Tadmor algorithm to evolve a relativistic 3+1 dimensional hydrodynamical system after it has reached local equilibrium. The work conducted to produce the results presented in this thesis is summarized in Fig. 1.1. This chapter will briefly introduce the topics, while a more detailed explanation of each component of this project will be developed in Chapter 2.

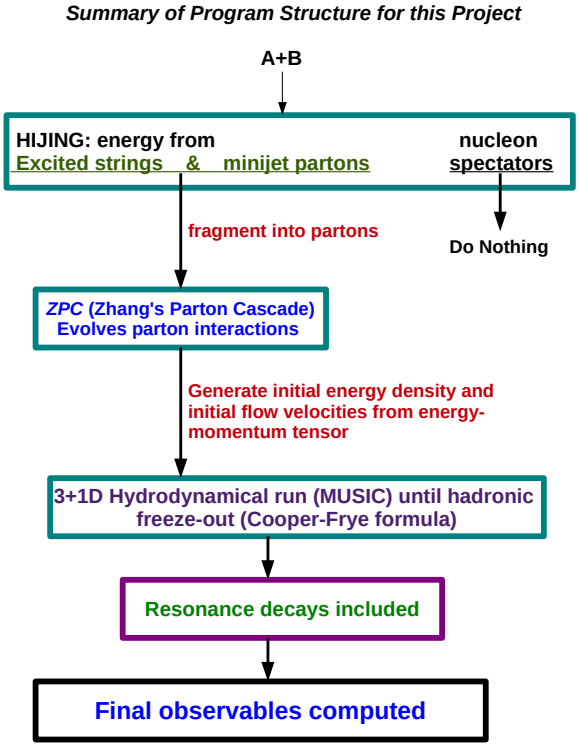

Figure 1.1: A brief summary of this project's numerical organization scheme, starting with the collision of two nuclei A and B.

The AMPT model uses initial geometric configurations and partonic interactions to produce the initial conditions of any two heavy ions colliding at relativistic energies. These two considerations (geometry and initial interactions) form the AMPT model's first two

components and they are run until the start time of the hydrodynamic evolution. The hydrodynamical evolution starts when the system reaches local thermodynamic equilibrium. Local thermodynamic equilibrium is defined locally and is characterized by the slow variation of intensive thermodynamic parameters of the system with respect to the other times of the system. Once the system reaches local thermodynamic equilibrium it is said to have thermalized.

The first of the AMPT model components is implemented using the HIJING model (Heavy Ion Jet Interaction Generator) and it produces the initial conditions which include the spatial and momentum distributions of minijet partons and soft excited strings [5]. Minijet partons are the partons produced from jets with high enough energies to move through the medium, but with energies lower than those of a jet. A jet is characterized by a stream of partons which move through the system with very high momentum compared to the rest of the system. AMPT includes minijets in its simulations and the result will be the presence of additional high momentum partons. Soft excited strings are the strings produced in the soft interactions between nucleons (protons or neutrons). These terms and conditions will be further discussed in Section 2.1.3. The initial positions of partons in each heavy nuclei are determined using the Glauber model. The Glauber model is a geometry-based model often used in heavy-ion simulations to determine how many nucleons collide in any single collision and the shape of the collision region based on the incorporation of experimental results [1]. The second of the AMPT components is the Zhang's Parton Cascade (ZPC) model and it is used to describe the scatterings among partons until the system is ready to be described by a hydrodynamic evolution. The finish point of this initial evolution is characterized by a significant reduction in the number of interactions between partons.

Once the partonic system has thermalized, one can reconstruct the initial energy-momentum tensor $T_0^{\mu\nu}$ over all space from spatial and momentum information. A quick program is then run to decompose $T_0^{\mu\nu}$ to extract the initial energy density ϵ_0 and the initial flow velocities u_0^μ. Each cell in the system is initialized with these initial values of ϵ_0 and u_0^μ. With these

initial values of energy density and flow velocity, the hydrodynamic model is run until the system reaches the freeze-out temperature T_{FO}. The freeze-out temperature is chosen by the programmer and is an approximation of the time needed for the system to reach temperatures cool enough for hadrons to start forming. Once the system freezes out at a constant freeze-out temperature, the energy density as a function of space is converted into hadrons using the Cooper-Frye formula. It is also possible to include the decay products of heavier, less stable, hadrons into more stable particles in MUSIC. From this point, one has information of the number of particles as a function of phase space and observables such as spectra, anisotropic flow components, average momentum distributions, and particle yields can be computed.

1.1 Motivation

Modeling the QGP would be difficult to do if one has to trace all particles in phase space. This many-body problem can instead be solved with a handful of variables and the hydrodynamic equations. The use of the hydrodynamical model in the description of heavy-ion collisions has been used since the time of Landau [16]. Landau wrote a series of lectures in 1953 on the use of a hydrodynamical solution to the nucleon-nucleon collision system—although, at the time the QGP was unknown and there was no data to confirm the use of the model in these systems [4, 17]. Hence, it was unclear that the simple and idealized laws of hydrodynamics can be applied.

Since then, many groups have done a great deal of work on theoretical modeling of hadron collisions at energies ranging from the Super Proton Synchrotron (SPS) energies to RHIC energies [2, 3, 4, 4, 4, 9, 18, 19, 20, 21, 22, 23, 24, 25, 26, 27, 28, 29, 30, 31, 32]. The first results of the heavy-ion experiments at the STAR (Solenoidal Tracker at RHIC) detector, from which significant momentum-space azimuthal anisotropic flow was observed was in 2001 [33]. Collective flow is the flow of matter which is highly interacting and, because of the initial collision geometry collision, the flow is anisotropic. A few months later, flow results which

roughly fit the Blast Wave model and a hydrodynamical model were published. Fits to the ideal hydrodynamical model calculations were set to reproduce the measured multiplicity and transverse momentum spectra [15, 33]. Hence, it was clear from these studies that the hydrodynamical model provides a good description of the evolution of QGP.

Since these first promising results, experimental measurement techniques and theoretical modeling became more sophisticated and the study of anisotropic flow—at the time only data for the dominant flow anisotropy was available—of different particle species was possible. The dominant flow of nuclei collisions corresponds to the overall shape of the overlap region; namely a flow described by an elliptic shape. This type of dominant flow is called elliptic flow. The measured anisotropic flow for different species showed a mass splitting which was predicted by the hydrodynamical model. Since all particles come from the same flow velocity field, different particles with common velocity implies that the elliptic flow at higher transverse momentum p_T for heavier particles corresponds to elliptic flow at lower p_T for lighter particles.

Until 2004, when the viscosity η to entropy s ratio in strongly coupled systems was calculated using the anti-de Sitter/conformal field theory model (AdS/CFT), viscosity was not included in hydrodynamical models. The prediction of η/s for an $N = 4$ super Yang-Mills quantum system in the strong coupling limit is $\eta/s = 1/4\pi$ [34]. Before this prediction, perturbative QCD and non-perturbative lattice QCD calculations of the viscosity coefficients were not available for strong coupling. With this calculation of η/s, viscous hydrodynamics more accurately described data compared to its ideal counterpart. Recently, a temperature dependent η/s and other inclusions such as bulk viscosity have been included in hydrodynamic computations [35].

While advancements on viscosity in the strong limit were made, experimental studies discovered the importance of fluctuations in the initial geometry configuration of Cu+Cu collisions. Cu+Cu collisions were used in 2005 to test whether the observed effects would differ from those of Au+Au collisions. If the initial geometry of the collision can be described

with a smooth nucleon distribution function in the overlap region then elliptic flow would be expected to be close to zero in the most central collisions ($b \approx 0$). However, it was observed that elliptic flow was large even in central Cu+Cu collisions. This pushed for a new definition of eccentricity where the shape of the overlap region was calculated using the positions of the fluctuating participants instead of the classical impact parameter. These developments will be further discussed in Section 2.

Fluctuations were also understood to be the reason why higher order anisotropic flow was non-zero. Although Sorensen predicted earlier that higher order odd harmonics could be significant [36], it was only in 2010 that there was real interest in their study [37]. The first results of higher order flow was made available in 2011 by the RHIC and LHC experiments and results for flow from the first to 6^{th} order were presented in that year's Quark Matter Conference [38]. The results showed that all of these flow coefficients were non-zero, with the values of the flow coefficients decreasing with increasing flow harmonic. This behavior is expected due to the decreasing nature of the initial eccentricities with increasing flow harmonic. Also, odd harmonics were found to have a weaker dependence on centrality. This is characteristic of the fluctuations of an initial globally symmetric geometry.

The power of a hydrodynamical model lies in its simplicity and general conditions, yet it is capable of capturing interesting features such as those present in the QGP medium produced in heavy ion collisions. The hydrodynamical model is simple because it is coarse-grained and the many-body system can be described by a handful of conserved charges and currents and an equation of state (EOS). The short-scale interactions of the particles are replaced by a thermodynamic description which is included in the EOS with the assumption that the system is in local thermodynamic equilibrium.

Global thermodynamic equilibrium exists in a closed system and is characterized by the homogeneity of the intensive parameters (such as temperature) throughout the entire system. In contrast, a system in local thermodynamic equilibrium assumes that the intensive parameters are functions of space-time, for instance the temperature, $T = T(t, x, y, z)$, but

that they vary slowly in a neighborhood of any point so that the system is described to be in thermodynamic equilibrium in a local sense [39]. Also, local thermodynamic equilibrium can exist in an expanding system such as those studied in this project.

There are three major numerical approaches to solving a hydrodynamical system. The first is the Lagrangian algorithm. This algorithm divides the initial fluid into cells which are allowed to move in space. These cells move with the fluid element they contain as the system evolves and expands. Another approach is the fixed grid (Eulerian) algorithm [25, 26, 40]. This approach divides the initial fluid into cells fixed in space and of equal size, and instead of following each cell around during the evolution, the algorithm looks into what is happening at each fixed cell as the fluid evolves and expands. The third approach is the smoothed particle hydrodynamic model which is discussed in References [9, 41]. This project employs an Eulerian (fixed-grid) algorithm.

Within the Standard Model, Quantum Chromodynamics (QCD) describes the strong interactions between quarks and gluons which ultimately determines the structure of hadrons and nuclei. QCD is a non-Abelian gauge theory and its two main features are asymptotic freedom and confinement [42]. Asymptotic freedom is the behavior that at small distances (or large momentum transfer) the effective strong coupling constant $\alpha_s(Q^2)$ decreases logarithmically as Q increases—hence, becoming larger as the distance increases. One interesting result of this observation is that quarks and gluons cannot exist in an unconfined state. This explains why quarks and gluons have not been observed individually. Because of asymptotic freedom, the short distance behavior of QCD can be described by perturbative QCD (pQCD) [43]. The behavior at large distances can be treated by lattice QCD calculations. Lattice QCD is a numerical scheme which evaluates Euclidean path integrals on a lattice. With realistic quark masses, QCD predicts that at very high temperatures and/or baryon densities a phase transition from hadronic matter to a matter of deconfined quarks and gluons will take place.

This matter expands and cools, as the temperature decreases after a few fm/c in relativis-

tic heavy ion collisions and quarks, and gluons start to combine into color-neutral particles (hadrons) [44]. The phase change of the hydrodynamic medium from QGP to a hadron gas is accounted for in the equation of state. This phase change is assumed to occur while the system remains in local thermodynamic equilibrium. The hadronic system further expands and cools, hardly interacting until particles reach the detectors. These hadrons carry information of the earlier history of the collision. The information one can extract about the earlier history is based on particle abundance and species, momentum distributions, and photons among others. It is here where experimental results are compared to theoretical predictions to produce a coherent description of the physics of heavy-ion collisions. These ideas will be further developed in what follows.

Choosing initial conditions which most closely describe the initial nuclei geometry, content, and dynamics before and right after collision is important. Any hydrodynamical model will evolve the specified initial conditions. Hence, a proper choice of representative initial conditions is essential. The conventional initial conditions chosen in 2+1D calculations are obtained from the boost invariant Glauber model. Boost invariance implies that there are no variations in energy density in the longitudinal direction—i.e. the direction perpendicular to the transverse area of the nuclei. These initial conditions have proven successful yet they lack many physical features of experimental data. Improvements on these initial conditions are used in 3+1D hydrodynamical models and include a Glauber model with fluctuations in the longitudinal direction, initial conditions known as IP-Glasma, and the AMPT initial conditions [5, 45, 46].

The initial conditions used in this project are the AMPT initial conditions and they are tested here for several reasons. These initial conditions have been successfully implemented by other groups [5, 6] and show promising results. Also, they have previously only been studied under an ideal hydrodynamical evolution and using them as input into a viscous hydrodynamical model has not been previously tested. In addition to including longitudinal fluctuations, AMPT also provides non-zero initial local flow velocities. This is an interesting

feature to include into MUSIC since previous simulations assumed no-flow initial conditions.

A summary of the current understanding of heavy ion collisions consists of the initial state of the nuclei (which is defined before the collision), the pre-equilibrium state which describes the time after collision but before the system reaches equilibrium, the QGP and hydrodynamical evolution stages during which interactions and particle production takes place, hadronization (which is the coalizing of quarks and gluons to form hadrons), and the hydrodynamical freeze-out after which particles do not interact. Depending on the initial relative geometry of nucleons, not all nucleons will participate in the collision. Since nuclei are moving at nearly the speed of light, the longitudinal length is Lorentz-contracted—giving the nuclei a pancake shape. The detail of particle interactions which occur in early heavy-ion collisions are not fully understood, although it is clear that nucleons break into their elementary constituents and particles are created due to the high energy of the collision. After hadronic freeze-out, the system consists of stable particles which can be detected experimentally. After a brief discussion of the purpose of this project, the different stages of heavy ion collisions will be discussed in more detail.

1.2 Purpose

The purpose of this project is to combine the initial conditions provided by AMPT and evolve them using MUSIC to produce observables which are comparable to data. Among other benefits, this work puts together more realistic initial conditions into MUSIC than most of what has been used previously. The common initial conditions are restricted to those provided by the Glauber model. Although these have been successful in reproducing some data, they lack many features which we know should be present in the initial conditions such as mini-jets and initial flow velocities. Furthermore, AMPT initial conditions have been used for ideal hydrodynamics but MUSIC provides a viscous correction to the evolution which more closely reflects a realistic hydrodynamical evolution. Combining these two features will

provide interesting ground for study of heavy-ion collisions. This work presents numerous results for heavy ion collisions with the with the use of improved numerical methods. The purpose of this work is to study the differences in a wide range of observables between fluctuating and non-fluctuating initial conditions and to couple these effects to ideal and viscous hydrodynamical evolution.

The collisions studied are for Au+Au nuclei colliding at a mid-central parameter value (30-40%). The impact parameter is the distance between the centers of the two nuclei and it defines the centrality of the collision. For example, a small impact parameter would imply that most of the transverse area of the nuclei overlap, while a large impact parameter implies that the nuclei have only a small overlapping region. Defining a collision in terms of its impact parameter b, number of participating nucleons N_{part}, or number of binary collisions N_{coll} characterizes the centrality class of the collision. The number of binary collisions is the number of collisions which occur between two nucleons, each from a different parent nucleus. Different centralities will produce different density profiles and final particle spectra based on the initial energy deposit in the collision system. The collision energy studied here is 200 GeV per nucleon-pair ($\sqrt{s_{\mathrm{NN}}} = 200$ GeV)—the same energy of experiments done at RHIC.

This thesis will cover the current theoretical foundation of ultra-relativistic heavy-ion collisions, the equation of state, initial conditions and the hydrodynamical model (with specific focus on MUSIC) in Chapter 2. Chapter 3 will cover the relevant input parameters and specific numerical choices which were made and Chapter 4 presents an extensive list resulting observables such as anisotropic flow components, spectra, total particle yields N, and mean-p_T values ($\langle p_T \rangle$). Finally, a summary and conclusion of this thesis will be given along with a thorough discussion of possible future work in Section 5.1.

Chapter 2

Theory

2.1 Heavy Ion Collisions

This section will describe the process of heavy-ion collisions, terminology and important features. It will then describe important components of MUSIC and AMPT models such as the equation of state, initial conditions, important assumptions, and interaction properties.

2.1.1 The History of a Heavy-Ion Collision

Before delving into a discussion of heavy-ion collision models, it is a good idea to develop a general understanding of the process at hand. The collision occurs between two ions (nuclei) which are accelerated to nearly the speed of light[1] before they collide. The location of each nucleon and the probability of two nucleons to collide from each nucleus is given by the Glauber model. After collision, the nucleons can be classified under two groups: the participants and spectators. As the names suggest, the participants are all the nucleons which collided and the spectators are all the nucleons which have passed each other without colliding. Once the nuclei collide, the spectators continue in the respective world lines at $v \sim 1$. Since the participants are made of more elementary particles and they collide at very

[1]Natural units are used throughout this thesis, $c = \hbar = k_B = 1$.

	τ_0 (fm/c)
RHIC $\sqrt{s_{\mathrm{NN}}} = 200$ GeV, $Au + Au$	0.4
LHC $\sqrt{s_{\mathrm{NN}}} = 2.76$ TeV, $Pb + Pb$	0.2

Table 2.1: τ_0 parameter values for two heavy ion systems.

high energy and momentum, the collisions are highly inelastic and they produce a rich shower of quarks and gluons which make up the QGP [47].

QGP is a fluid because it responds to pressure differences by flowing in the direction of lower pressure. In 2005, the RHIC experiments claimed that they had created the most "perfect fluid" ever made, with the lowest possible specific viscosity or η/s ratio [16, 43]. The formation of QGP between collision time and $\tau_0 \sim 0.2 - 0.4$ fm is not completely understood. However groups such as [5] have produced models which describe the process by considering the production and interaction properties of excited strings and mini-jet partons which occur before thermalization.

After the stated proper time, the system is assumed to have reached thermodynamic equilibrium and hydrodynamic expansion becomes applicable. The choice of initial proper time τ_0 partially depends on the system in question (Table 2.1 shows different systems and the choice of τ_0 according to [6]) and partly depend on the type of research direction that one is interested in. Hence, τ_0 is conventionally a parameter in hydrodynamical models (including MUSIC).

While the medium expands and cools, it reaches a point when there are no longer inelastic collisions between its constituents. This point in the evolution is characterized by the freeze-out temperature T_{FO} or freeze-out energy density ϵ_{FO}. The system is no longer dense once it reaches T_{FO} and local thermalization breaks down (i.e. the mean free path is large) so the hydrodynamic evolution has to be cutoff. This is done by-hand at a chosen freeze-out temperature [4]. After freeze-out, hadrons evolve via free-streaming—rarely interacting until they reach the detector. Since the hadrons are the particles which reach the detectors, they are studied extensively so that the total evolution of the system may be understood. In

addition to the hadrons, photons created in the high-energy process are also detected. Since photons rarely interact, they also contain clues into the early evolution history (for example, see References [48, 49, 50, 51, 52]).

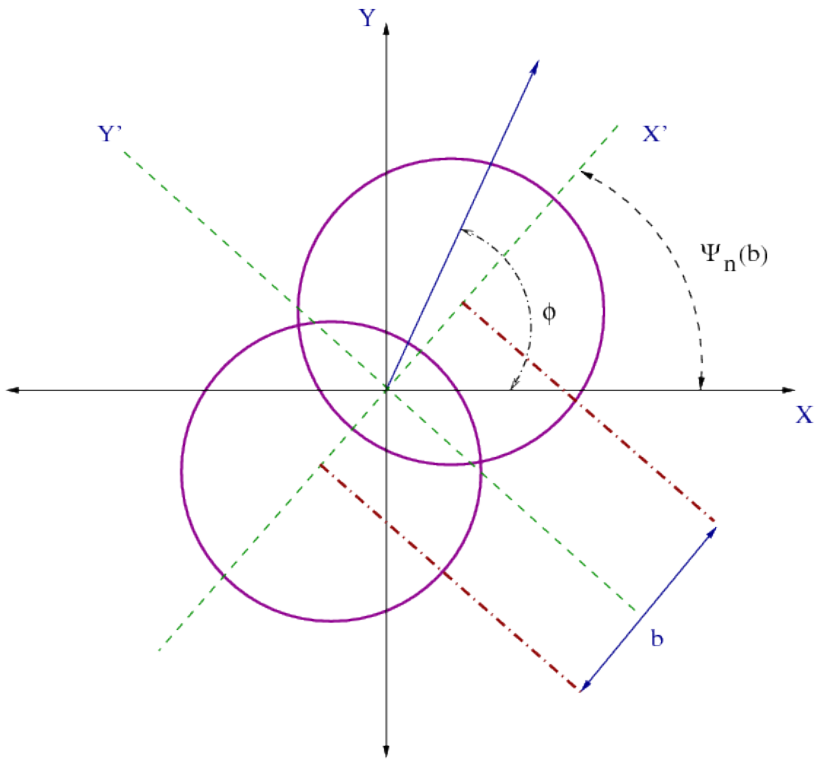

Figure 2.1: The collision geometry of a non-central collision as seen in the transverse plane is shown. The transverse plane is defined by the (X', Y') axis, and ϕ is the azimuthal angle of an outgoing particle. The impact parameter is defined as the distance between the centers of the nuclei.

The impact parameter is defined as the distance between the two centers of the nuclei in the transverse plane, where the respective radii are given by R_1 and R_2. The transverse plane is defined to be perpendicular to the reaction plane, which is defined in terms of the impact parameter vector and the beam axis usually chosen to be the z-axis. Probabilistically, collisions usually happen for $0 < b < R_1 + R_2$. It is experimentally possible to have collisions outside of this range, however, theoretically the AMPT model is given a specific range of impact parameters from which one value is chosen at random so that the nuclei do not pass each other without colliding. Hence, for the purposes of this project, the total impact

parameter range will be restricted to the above. The collisions for which b is small are central collisions and large-b collisions are peripheral collisions. The geometry formed by the region of collision will characterize the type of flow which occurs and also the number of particles produced. For central collisions the flow is mostly isotropic and for non-central collisions the flow is anisotropic due to the initial "almond shaped" geometry.

Fig. 2.1 depicts a typical non-central collision with transverse plane Ψ_n defined by the X' and Y' axis. The impact parameter axis conventionally defines the x-direction and the y-direction is the perpendicular axis to it constrained on the transverse plane. The transverse plane can generally be off-axis with respect to the laboratory plane (X, Y).

2.1.2 Anisotropic Flow

Anisotropic flow is a prominent feature of heavy-ion collisions. At first, it was believed that QGP was a weakly interacting medium. A weakly interacting medium has small cross-sections and large mean free paths (i.e. the distance between two consecutive collisions), whereas a highly interacting system is dense and has a short mean free path. The elliptical flow coefficient is expected to be small in a weakly interacting medium with equal expansion in the x and y directions. This would be true even in non-central collisions. However, if the medium were highly interacting, the flow would be larger in the direction of the short axis and smaller in the direction of the long axis.

The reason for this behavior arises from the fact that the nuclei roughly have a uniform transverse density before collision so that after the collision the pressure would be the same in the x and y directions. However, since $\Delta x < \Delta y$ the pressure gradient would be larger in the x-direction, causing $\frac{\Delta P}{\Delta x} > \frac{\Delta P}{\Delta y}$, and so the fluid will pick up a larger momentum in the x-direction due to the larger pressure gradient. This will cause v_2 to be larger than that for a weakly interacting fluid and this is exactly what is observed. The elliptic flow coefficient

v_2 is defined as the comparison of flow measured along the short and long axes,

$$v_2 \equiv \frac{\langle p_x^2 - p_y^2 \rangle}{\langle p_x^2 + p_y^2 \rangle}, \tag{2.1}$$

where p_i is the momentum along the stated transverse direction, and the $\langle ... \rangle$ indicates the average over particles and events [53]. Even if the transverse density were non-uniform, the changes in pressure in the x-direction would have a larger gradient than those in the y-direction, and so will cause similar elliptic flow. As another example, a system of ultra-cold ^{6}Li atoms released from a laser trap expands in a similar flow pattern to QGP.

The complete spectrum of anisotropic flow (directed v_1, elliptic v_2, triangular v_3, etc.) can be quantified in the following way. Anisotropic flow is a measure of the correlation between anisotropy in particle momentum distributions and the transverse plane Ψ_n. The transverse plane is a function of the harmonic being measured and the impact parameter of the collision. The various patterns of anisotropic flow can be extracted with a Fourier expansion of the invariant triple differential distribution of an outgoing particle

$$E\frac{d^3N}{d^3\boldsymbol{p}} = \frac{1}{2\pi}\frac{d^2N}{p_T dp_T dy}\left(1 + 2\sum_{n=1}^{\infty} v_n \cos[n(\phi - \Psi_n)]\right), \tag{2.2}$$

where E is the energy of the particle, p_T is the transverse momentum, y is the rapidity, ϕ is the azimuthal angle of an outgoing particle with $\phi = \tan^{-1}\left(\frac{p_y}{p_x}\right)$, and Ψ_n is the transverse plane angle with respect to the laboratory frame of the n^{th} harmonic. Multiplying the left hand side by the energy of the particle allows one to use the dynamical rapidity y instead of momentum p_z. Each term in the expansion sum over n gives a flow coefficient for a certain geometry of flow, starting with directed flow ($n = 1$), elliptic flow ($n = 2$), triangular flow ($n = 3$), etc. The Fourier coefficients, v_n, depend on transverse momentum and rapidity and are given by

$$v_n(p_T, y) = \langle \cos n(\phi - \Psi_n) \rangle \,. \tag{2.3}$$

The average is taken over particles, averaged and events and is given in the (p_T, y) bin

specified [19, 54]. Ψ_n is the transverse plane angle of the n^{th} harmonic and is defined through the angle ϕ as

$$\Psi_n = \frac{1}{n}\tan^{-1}\left(\frac{\langle\sin(n\phi)\rangle}{\langle\cos(n\phi)\rangle}\right). \tag{2.4}$$

The average in the Ψ_n computation is not weighted by p_T as is done in some works [9] because the flow analysis will be done for low p_T since this is the region where hydrodynamics is valid. At transverse momenta $p_T \geq 2$ GeV, hydrodynamics is considered to no longer be valid. Current improved viscous hydrodynamical models with fluctuating initial conditions produce results that are in close agreement to flow measurements at RHIC and the LHC and can also reproduce v_2 to v_4 event-by-event distributions measured by the ATLAS collaboration [15, 55].

The definition of the transverse plane in terms of symmetry axis for each harmonic, Ψ_n, is an approximation which was previously used and is only valid for uniform transverse parton density. However, for models which include transverse fluctuations, the definition of the transverse plane depends on the number of participating nucleons as well as their positions. As a consequence of these fluctuations, the transverse plane could very well shift from the symmetry axis and should be corrected for. The formulation above describes a particle-dependent transverse plane and is used in MUSIC for flow calculations.

2.1.3 Soft and Hard Sector

MUSIC is primarily a program which treats the relativistic hydrodynamic evolution of the dense fluid produced in heavy-ion collisions. However, there are certain situations where jet contributions (which are not considered as part of the medium evolution due to their different propagation properties and momenta) are non-negligible and should be accounted for. The main purpose of including jets is that they account for extra energy deposit in the medium as jets move outwards with high momentum. The energy deposit is due to the jet interactions with the medium and is referred to as jet quenching [56, 57].

The system produced in heavy ion collisions can be divided into the soft and hard sectors.

The dense nuclear medium of particles is the soft sector [58] and jets make up the hard sector. In MUSIC, the soft and hard sector are differentiated by imposing a constraint on the range of transverse momenta. The soft sector interactions are observed for $p_T \lesssim 1$ GeV (low-p_T) while the hard sector sector satisfies $p_T \gtrsim 2$ GeV (high-p_T). In this project, jets (and hence jet quenching [56, 57, 59]) have been turned off in the hydrodynamical simulations since they are not the focus of this study. However, the initial conditions carry information on the propagation of mini-jets (with 1 GeV $\lesssim p_T \lesssim$ 2 GeV) and so this information will get carried through the hydrodynamical evolution. The effect of mini-jets is to increase the energy of the medium and their presence at the end of the evolution might be strong enough to be detected in correlation functions.

2.1.4 Baryon Density: A Practical Assumption

Baryon number density or mass density, n_B or ρ_B, are usually assumed to be zero. This is a reasonable assumption since the participants contribute a relatively small baryon number compared to the number of quark-anti-quark pairs produced. It is guaranteed that this number is large since the collision is relativistic and also because Au+Au collisions are large enough to produce many particles with an approximately zero baryon density, since the number of produced quarks and anti-quarks (produced in equal numbers) outnumbers the number of valence quarks initially present in the nucleons. Hence, it is a common approximation to set $n_B = 0$ [6, 9, 10, 11, 12, 16].

One may reasonably argue that the recoiling nuclei (carrying with them the spectators) will contribute a non-negligible amount to the baryon density since they are still in the vicinity of the collision. However, since the recoiling nuclei are moving at nearly the speed of light they are near the beam rapidity. Hence, they are out of the experimentally detectable range. With the assumption that the baryon density (or the baryon chemical potential) vanishes, the conservation equations decouple.

2.2 Theoretical and Numerical Aspects

This section will develop the hydrodynamical model as it is used in heavy-ion collision dynamics and discusses some important formulae and numerical methods used in the MUSIC and AMPT models.

2.2.1 The Ideal (3+1)D Relativistic Hydrodynamical Model

This section discusses the structure of MUSIC. This will include a discussion of the conservation equations, the requirement of an equation of state (EOS), our choice of coordinate system, some important numerical methods, the freeze-out method, and resonance decays. This section will first discuss the formulation of an ideal hydrodynamical model, after which shear viscosity will be included as a correction to the ideal case. The viscous correction also satisfy the conservation equations and causality.

Results at CERN showed that there exists a "central-plateau" in the particle production as a function of rapidity for hadron-hadron and nucleon-nucleus collisions [60, 61]. These results motivated the use of a (2+1)D model to approximate the (3+1)D collision at mid-rapidity for nucleus-nucleus collisions [62]. Since then, much work has been done on the (2+1)D hydrodynamical model [4, 28, 63, 64, 65] and the results compared very well to some data. However, an (3+1)D hydrodynamical model is needed for a more realistic description of data. For example, at SPS energies, the central plateau region for heavy ion collisions is not very pronounced and looks more like a Gaussian peak. In addition to this, the motivation is to also investigate the effects of non-trivial longitudinal dynamics on observables.

Devising an (3+1)D model is not as simple as adding an extra dimension to an (2+1)D model. The proper longitudinal dynamics and the requirement of properly adding viscosity come into play. Adding viscosity to the conservation equations includes adding viscous corrections and also using a formalism which controls the faster-than-light propagation of information. The Israel-Stuart formalism avoids this nonphysical propagation [27, 66, 67, 68].

A variant of this formalism is used in MUSIC to control this behavior. The ideal hydrodynamical equations will be covered first.

The conservation equations of energy-momentum which describe the expansion of dense and hot matter created after two relativistic heavy ions collide are

$$\begin{aligned} \partial_\mu T^{\mu\nu} &= 0, \\ \partial_\mu J^\mu_B &= 0. \end{aligned} \tag{2.5}$$

J^μ_B is the baryon current and $T^{\mu\nu}$ is the energy-momentum tensor. These equations are local, with no additional sources of energy, momentum, and baryon current after the collision time. The indices μ, ν take the values $0, 1, 2, 3$. The components of the energy-momentum tensor physically describe

$$\begin{aligned} T^{00} &= \text{ energy density}, \\ T^{ij} &= \text{ momentum flux, } i, j = \text{ 1, 2, 3}, \\ T^{i0} &= \text{ energy flux along the } i^{th} \text{ axis}, \\ T^{0j} &= \text{ density of the } j^{th} \text{ component of momentum.} \end{aligned}$$

In the rest frame of the fluid, since there is no flux of energy and momentum, $T^{i0} = T^{0j} = 0$ and $T^{00} = \epsilon$, where ϵ is the energy density. Also, the fluid is isotropic in this frame and so $T^{ij} = P\delta^{ij}$, where P is the thermodynamic pressure. The energy-momentum density tensor is therefore

$$T^{\mu\nu}_{\text{rest}} = \begin{pmatrix} \epsilon & 0 & 0 & 0 \\ 0 & P & 0 & 0 \\ 0 & 0 & P & 0 \\ 0 & 0 & 0 & P \end{pmatrix} \tag{2.6}$$

and $J^\mu_{\text{rest}} = 0$ in this frame. Now, to boost $T^{\mu\nu}$ in any frame, we define the local 4-velocity u^μ in each hydrodynamical cell. The boosted quantities become

$$T^{\mu\nu} = (\epsilon + P)u^{\mu}u^{\nu} - Pg^{\mu\nu}, \tag{2.7}$$

$$J^{\mu}_{B} = n_{B}u^{\mu}, \tag{2.8}$$

where $g^{\mu\nu}$ is the metric tensor with the signature $g_{\mu\nu} = (1, -1, -1, -1)$, and u^{μ} satisfies the normalization condition[2] $u^{\mu}u_{\mu} = 1$.

In a relativistic model it is inconvenient to use Minkowski coordinates. Boost invariance becomes difficult to deal with in this coordinate system and the most natural time parameter is the proper time $\tau = \sqrt{t^2 - z^2}$. As the system evolves it follows a different line of constant proper time. The system freeze-out occurs at $\tau = \tau_{\rm FO}$. With proper time making one axis, the orthogonal axis to proper time is the spatial pseudo-rapidity η_s which follows linear lines starting at the $z = t = 0$ origin. Hence, it is conventional to use the (τ, x, y, η_s) coordinate system. The coordinate transformation is given by

$$t = \tau \cosh(\eta_s), \tag{2.9}$$

$$z = \tau \sinh(\eta_s), \tag{2.10}$$

where τ is the longitudinal proper time defined as $\tau = \sqrt{t^2 - z^2}$ and η_s is the space-time rapidity. One can also use an alternate definition (these are equivalent) [69]

$$\tau = \sqrt{t^2 - z^2}, \tag{2.11}$$

$$\eta_s = \frac{1}{2}\ln\frac{t+z}{t-z}. \tag{2.12}$$

Changing from the Minkowski coordinate system to the $\tau - \eta$ coordinate system changes the metric structure to have an τ dependence $g^{\mu\nu} = (1, -1, -1, -1/\tau^2)$. The η-index definitions of equations given in this paper are not the usual definitions of curvilinear system tensors. The definition used here, and in MUSIC, takes the η-index factor $1/\tau^2$ out of the metric and carries it instead in the η-index of tensors. This is done for two reasons: to have

[2]It is worth noting that MUSIC uses a mostly positive metric in its coding program. Hence, for example, the velocity normalization condition would read $u^{\mu}u_{\mu} = -1$, or, $u_{\tau}^2 = 1 + u_x^2 + u_y^2 + (1/\tau^2)u_{\eta_s}^2$ in the latter metric convention.

a constant metric and so that the length unit of all η_s components corresponds to those of the other 3 dimensions.

Other useful variables in this coordinate system include the dynamical rapidity

$$y = \tanh^{-1} \frac{p^z}{p^t}, \tag{2.13}$$

and so one can write momentum as [70],

$$p^t = m_T \cosh y, \qquad p^z = m_T \sinh y. \tag{2.14}$$

The variable m_T is the transverse energy of the particle and is defined by $m_T = \sqrt{m^2 + p_T^2}$. Rapidity is additive in the $\tau - \eta_s$ coordinates with boosts along the z-direction [47].

The conservation equations (2.5) will have to be transformed in each index. The result of the transformations are shown below [9, 10]. Conservation of baryon current density takes the form

$$\partial_\tau(\tau J^\tau) + \partial_{\eta_s}(J^{\eta_s}) + \partial_v(\tau J^v) = 0, \tag{2.15}$$

where the boosted currents are given by

$$\begin{aligned} J^\tau &= (\cosh \eta_s J^0 - \sinh \eta_s J^3), \\ J^{\eta_s} &= (\cosh \eta_s J^3 - \sinh \eta_s J^0). \end{aligned} \tag{2.16}$$

The above baryon currents are Lorentz boosted with space-time rapidity $\eta_s = \tanh^{-1}(z/t)$. The components of the charge current J^v is the unboosted transverse components J^x and J^y. Conservation of energy-momentum tensor is

$$\begin{aligned} \partial_\tau(\tau T^{\tau\tau}) + \partial_{\eta_s}(T^{\eta_s\tau}) + \partial_v(\tau T^{v\tau}) + T^{\eta_s\eta_s} &= 0, \\ \partial_\tau(\tau T^{\tau\eta_s}) + \partial_{\eta_s}(T^{\eta_s\eta_s}) + \partial_v(\tau T^{v\eta_s}) + T^{\tau\eta_s} &= 0, \\ \partial_\tau(\tau T^{\tau v}) + \partial_{\eta_s}(T^{\eta_s v}) + \partial_w(\tau T^{wv}) &= 0, \end{aligned} \tag{2.17}$$

where v and w each runs over the transverse coordinates x and y. It is important to differenti-

ate between the transverse and longitudinal directions because fluctuations in the longitudinal direction are independent of those in the transverse direction and also because the nature of the flow is different in the longitudinal and transverse directions.

The hydrodynamical model can be solved if one finds a solution to the above conservation equations. In order for the solution to have any physical meaning it is required that the system of equations be closed. This implies that there should be 5 variables (degrees of freedom—DOF) to complete the description of the set of conservation equations. Eq.(2.8) makes reference to the energy density $\epsilon(x)$, thermal pressure $P(x)$, 4-velocity u^μ, and baryon density n_B. This is a total of 6 DOF taking into account the normalization condition on u^μ. Hence, there is one more condition required to close the system of equations, and this is the equation of state (EOS) [22]. The EOS gives an expression for the pressure in terms of energy density and baryon density $P = P(\epsilon, \rho_B)$. The EOS is the subject of Section 2.2.3.

The above 5 differential equations are solved with the Kurganov Tadmor (KT) algorithm. The KT scheme is run at each time step to solve for $T^{\tau v}$, $T^{\tau\tau}$, $T^{\tau\eta_s}$, and J^τ using Heun's rule [9, 10]. The KT scheme solves differential equations of the following general form

$$\partial_t \rho_a = -\nabla \cdot \vec{\boldsymbol{J}}_{\boldsymbol{a}}, \tag{2.18}$$

where $a = 0...4$ runs through energy, momentum, and baryon density.

Solving this system of equations with the naïve discritization method introduces instabilities [9] which increase with each time step. The Lax method [71] is one algorithm which avoids these instabilities by introducing a second order numerical viscosity. The differential equation Eq.(2.18) is written in terms of the time step Δt and spatial steps $\Delta\vec{x}$. In 1+1 dimensions this correction reads

$$\partial_t \rho_a = -\partial_x J + \Big(\frac{(\Delta x)^2}{2\Delta t}\Big)\partial_x^2 \rho. \tag{2.19}$$

The second term should be kept small and this is done is by imposing the condition that as

Δt decreases Δx also decreases. This will affect computation time depending on the size of Δt and one would ideally want a stable solution which is independent of the size of time step used and which also allows for a time step size independent of the spatial step size. The KT method offers such a solution.

The KT method is a finite volume method which defines the average density at each cell centered at x_j with a width of Δx. In 1-D, the finite volume method rewrites Eq.(2.18) as

$$\frac{d}{dt}\overline{\rho}(t) = \frac{J(x_{j-1/2}, t) - J(x_{j+1/2}, t)}{\Delta x}. \tag{2.20}$$

The average density $\overline{\rho}(t)$ is computed between the halfway points $x_{j\pm1/2}$. However useful, this method introduces ambiguities at the half-way points. To fix this problem, a maximum local propagation speed less than the speed of light is introduced at every time step to determine how far the shock wave due to the discontinuity at the half-points (i.e. where J is evaluated) can travel. The local propagation speed is given by $a = |\partial J/\partial\rho|$. The final result of the KT method in one spatial dimension for the conservation equation in the limit $\Delta t \to 0$ is

$$\frac{d}{dt}\overline{\rho}(t) = -\frac{H(x_{j+1/2}, t) - H(x_{j-1/2}, t)}{\Delta x}, \tag{2.21}$$

where

$$\begin{aligned} H_{j\pm1/2} =& \frac{J(x_{j\pm1/2,+}, t) + J(x_{j\pm1/2,-}, t)}{2} \\ & - \frac{a_{j\pm1/2}(t)}{2}\big(\overline{\rho}_{j\pm1/2,+}(t) - \overline{\rho}_{j\pm1/2,-}(t)\big), \end{aligned} \tag{2.22}$$

with

$$\overline{\rho}_{j+1/2,+} = \overline{\rho}_j - \frac{\Delta x}{2}(\rho_x)_{j+1}, \tag{2.23}$$

$$\overline{\rho}_{j+1/2,-} = \overline{\rho}_j + \frac{\Delta x}{2}(\rho_x)_j, \tag{2.24}$$

and

$$x^n_{j\pm1/2,\pm} = x_{j\pm1/2} \pm a^n_{j\pm1/2}\Delta t. \tag{2.25}$$

From the above expressions, it is only left to specify the spatial derivative $(\rho_x)_j$. One can use several methods. MUSIC uses a stable and consistently non-oscillatory (i.e. even for large gradients) minmod limiter solution given by [9, 72]

$$(\rho_x)_j = \text{minmod}\left(\theta\,\frac{\overline{\rho}_{\text{j+1}} - \overline{\rho}_{\text{j}}}{\Delta\text{x}}, \frac{\overline{\rho}_{\text{j+1}} - \overline{\rho}_{\text{j-1}}}{2\Delta\text{x}}, \theta\,\frac{\overline{\rho}_{\text{j}} - \overline{\rho}_{\text{j-1}}}{\Delta\text{x}}\right). \tag{2.26}$$

The parameter θ is chosen to be 1.8 in this project following [73]. This method can easily be generalized to 3-spatial dimensions using the method of operator splitting.

The following energy-momentum tensor decomposition (in 3-spatial dimensions in $\tau - \eta$ coordinates)

$$\begin{aligned}
T^{\tau\tau} &= (\epsilon + P)u^\tau u^\tau - P,\\
T^{\tau\eta_s} &= (\epsilon + P)u^{\eta_s} u^\tau,\\
T^{\tau v} &= (\epsilon + P)u^\tau u^v,\\
J^\tau &= \rho u^\tau,
\end{aligned}$$

and the EOS, which provides us with $P = P(\epsilon, \rho)$, form a set of closed decomposition equations which determine the energy density ϵ, baryon density ρ, and the thermodynamic pressure P. The flow velocity components satisfy the same Lorentz boosted form as in Eq.(2.16)

$$\begin{aligned}
u^\tau &= (\cosh\eta_s u^0 - \sinh\eta_s u^3),\\
u^{\eta_s} &= (\cosh\eta_s u^3 - \sinh\eta_s u^0).
\end{aligned} \tag{2.27}$$

The transverse components of the flow velocity are unchanged. Written out explicitly, the energy density and baryon density are solved at every space point using the following coupled

equations

$$\epsilon = T^{\tau\tau} - \frac{K}{(T^{\tau\tau} + P(\epsilon, \rho))}, \tag{2.28}$$

$$\rho = J^{\tau}\sqrt{\frac{\epsilon + P(\epsilon, \rho)}{T^{\tau\tau} + P(\epsilon, \rho)}}, \tag{2.29}$$

where $K = (T^{\eta_s\tau})^2 + (T^{v\tau})^2 + (T^{w\tau})^2$. Once the energy and baryon density are determined, the spatial components of the flow vector are given by

$$u^i = \frac{T^{\tau i}}{(\epsilon + P)u^{\tau}}. \tag{2.30}$$

Heun's rule applied to the hydrodynamical equations solves differential equations of the following general form

$$\frac{d\rho}{dt} = f(t, \rho), \tag{2.31}$$

and it provides a computational method for the quantity ρ of the next time step by using a second order approximation method from the previous time step. With these values of ϵ, ρ, P, and u^{μ}, the whole ideal $T^{\mu\nu}$ can be reconstructed and used in the next time step [9]. The subject of viscous hydrodynamics will be discussed in Section 2.2.2.

As discussed above, the KT method allows us to solve the general differential form given in Eq.(2.18) with an arbitrary time step. However, due to the numerical time integration scheme, the Courant-Friedrichs-Lewy condition (CFL) [74] imposes a condition on Δt. In MUSIC, this condition is given as a constraint on the proper time step $\Delta\tau$

$$\Delta\tau < min\Big(\frac{\Delta x}{10}, \tau_0\frac{\Delta\eta_s}{10}\Big), \tag{2.32}$$

where Δx is the cell size in the transverse directions in units of fm, and $\Delta\eta_s$ is the cell size in the η_s-direction and is unit-less.

2.2.2 The Viscous Hydrodynamical Model

Including viscosity in the hydrodynamical model changes the evolution of the system in several ways. Viscosity creates a longer lasting QGP phase, changes the flow velocities of the fluid, changes the temperature profile evolution, and even affects other components of the model such as photon production [75]. In an ideal evolution, the flow of two fluid layers are independent of each other, however, in viscous hydrodynamics the flow in one cell will affect the flow in neighboring cells.

The resulting dissipation between fluid layers creates extra entropy in the system. In other words, including viscosity implies that the tangential force between fluid elements is non-zero so that neighboring fluid cells will dissipate energy to each other.

In this work, the inclusion of shear viscosity in the hydrodynamical evolution will be discussed, however, bulk viscosity is omitted for simplicity. In the first order viscous (3+1)D hydrodynamical model, the conservation equations take the usual form $\partial_\mu T^{\mu\nu} = 0$ and $\partial_\mu J^\mu = 0$, where $T^{\mu\nu}_{\text{ideal}}$ is given by Eq.(2.8). The corrected energy-momentum tensor to first order in shear viscosity is given by

$$T^{\mu\nu} = T^{\mu\nu}_{\text{ideal}} + S^{\mu\nu}, \tag{2.33}$$

$$S^{\mu\nu} = \eta\Big(\nabla^\mu u^\nu + \nabla^\nu u^\mu - \frac{2}{3}\Delta^{\mu\nu}\nabla_\alpha u^\alpha\Big), \tag{2.34}$$

where η is the shear viscosity and the tensors $\Delta^{\mu\nu}$, ∇^ν are defined as

$$\Delta^{\mu\nu} = g^{\mu\nu} - u^\mu u^\nu \tag{2.35}$$

$$\nabla^\nu = \Delta^{\mu\nu}\partial_\nu. \tag{2.36}$$

The above formulation turns out to be problematic because it leads to a diffusion equation. In other words, causality is not necessarily obeyed in the above [73, 76, 77]. The solution to this problem is given by the Israel-Stewart viscous correction formalism. To solve the above causality problem a relaxation time τ_π, which allows the system to relax in a finite amount of time, is introduced and the equations are corrected to second order in gradient

$$T^{\mu\nu} = T^{\mu\nu}_{\text{ideal}} + W^{\mu\nu}, \tag{2.37}$$

where the new tensor $W^{\mu\nu}$ satisfies [27, 34]

$$\Delta^{\mu}_{\alpha}\Delta^{\nu}_{\beta}u^{\alpha}\partial_{\sigma}W^{\alpha\beta} = -\frac{1}{\tau_{\pi}}(W^{\mu\nu} - S^{\mu\nu}) - \frac{4}{3}W^{\mu\nu}(\partial_{\alpha}u^{\alpha}). \tag{2.38}$$

The effects of shear viscosity on spectra, flow, and mean-p_T will be discussed in Section 4.

2.2.3 Equation of State

As stated before the equation of state (EOS) closes the system of hydrodynamical equations. The EOS should contain the complex thermodynamic processes and include a transition from QGP to hadron gas. The choice made here, and in many other works, is the Houvinen-Petreczky EOS with zero chemical potential [78]. This EOS gives a relation for pressure as a function of energy density, and the parametrization used here is given the label s95p-v1. The "s95" defines the fraction of ideal entropy reached relative to the Stephan-Boltzmann equation. Hence, in this case, the entropy density reaches 95% of its Stephan-Boltzmann value. The letter "p" states the type of parametrization, and "v1" indicates the version [78].

This equation of state is a good choice for several reasons. Since calculations show that the hydrodynamical fluid is not very far from an ideal fluid, choosing an EOS which deviates from the ideal case by $5 - 15\%$ is common in hydrodynamical calculations [12, 78]. In the high temperature regime, the fluid is modeled using a non-interacting gas of massless u, d and s quarks and gluons subject to an external bag pressure [9]. At low temperatures, below the cross-over temperature of about $T_{\text{crit}} = 164$ MeV the medium is modeled as a hadron resonance gas (HRG) with all resonances included up to 2 GeV [79].

2.2.4 Hadronic Freeze-out

QGP continues interacting until the medium expands and cools enough for the quarks and gluons to coalesce into hadrons. After hadrons are formed, it is believed that the particles

follow free streaming flow (i.e. they do not interact). It was mentioned above that the process during which hadrons form is assumed to occur at a certain freeze-out temperature, T_{FO}. Since the hadrons are the particles which can be detected, it is of high importance to be able to predict the number of each type of particle produced in the collision. If this prediction can be done with enough accuracy to describe data then it can be concluded that the model choice, choice of EOS, parameter values, and the initial conditions form a valid description.

The three-dimensional hypersurface on which the particle counting is performed is denoted $\Sigma(x)$ and is a function of 4-dimensional space-time and will be denoted $\Sigma^{\mu}(\vec{x})$ in general orthogonal coordinates. It can be shown that the overall shape of hypersurface can take on many forms as long as it closes off the future light-cone whose origin is the collision point [80]. The number of particles of type i which cross an infinitesimal surface element $d^3\Sigma_\mu$ can be computed by taking the scalar product of Σ_μ with the 4-current density of particle i at point x, denoted $d^3\Sigma_\mu(x)j_i^\mu(x)$. The total number of particles is then the integral over the entire hypersurface

$$N_i = \int_\Sigma d^3\Sigma_\mu(x) j_i^\mu(x) = \int_\Sigma d^3\Sigma_\mu(x) \bigg(\int \frac{d^3p}{(2\pi)^3 E}\, p^\mu f_i(x,p) \bigg), \tag{2.39}$$

where $E = E(m,p)$ is the energy.

In the second equality the particle 4-current density is given as the integral over the particle momenta with velocity $\frac{p^\mu}{E}$ and the Lorentz-invariant particle phase-space distribution function $f_i(x,p)$.

Using the dynamic-rapidity variable, the momentum measure d^3p/E is given by

$$dy\, p_T\, dp_T\, d\phi_p = dy\, m_T\, dm_T\, d\phi_p, \tag{2.40}$$

where ϕ_p is the azimuthal angle of $\vec{p_T}$, and m_T is the transverse energy of the i^{th} particle and satisfies $m_T = \sqrt{m^2 + p_T^2}$ where m is the mass of the particle.

From Eq.(2.39), we get the Lorentz invariant Cooper-Frye formula for the momentum distribution for particle species i

$$E\frac{dN_i}{d^3p} = \frac{dN_i}{dy\, p_T\, dp_T\, d\phi_p} = \frac{dN_i}{dy\, m_T\, dm_T\, d\phi_p} = \frac{1}{(2\pi)^3}\int_\Sigma p\cdot d^3\Sigma(x) f_i(x,p). \tag{2.41}$$

The number of particles counted should not depend on the reference frame of the observer. The Cooper-Frye procedure for converting the hydrodynamical fluid into particles conserves energy, momentum, and charge without any other specific considerations given that the EOS of the fluid is the same as the EOS of free particles (hadrons in this case) [78]. This is the formula which is usually used in hydrodynamical models to reconstruct particles at freeze-out.

It can be shown that two different hypersurfaces Σ_1 and Σ_2 give the same particle number for each species, if the distribution function $f_i(x,p)$ between the two surfaces evolves via a Boltzmann equation with a collision kernel that preserves the particle number for each species from Σ_1 to Σ_2 [80]. With a distribution function which satisfies this condition, one is sure that if a freeze-out surface is found, the surface can be shrunk until the smallest and earliest such surface which encloses all the scattering processes [80]. It can also be shown that one obtains the same momentum spectra if the system evolves between Σ_1 and Σ_2 via free-streaming. This last requirement imposes that the solution of $f_i(x,p)$ is a solution of the collisionless Boltzmann equation. The equilibrium solution satisfying the above two conditions can be written in the following form [9, 12]

$$f(u^\mu p_\mu) = \frac{g_i}{(2\pi)^3}\,\frac{1}{\exp((u^\mu p_\mu - \mu_i)/T_{FO}) \pm 1}, \tag{2.42}$$

where g_i is the particle spin and isospin degeneracies, the Boltzmann distribution function is evaluated at constant temperature $T_{\rm FO}$, and the $\pm$ takes care of particle statistics (the minus sign for bosons and plus sign for fermions). The particle energy in the rest frame is $u^\mu(x)p_\mu$ and μ_i is the chemical potential of each particle. The 4-velocity u^μ here denotes the velocity of the fluid on the freeze-out hypersurface.

The Boltzmann distribution function corrected for finite viscosity [11] is included as a perturbation to the ideal function $f = f_0 + \delta f$ with

$$\delta f = f_0(1 \pm f_0) p^\alpha p^\beta W_{\alpha\beta} \frac{1}{2(\epsilon + P)T^2}, \tag{2.43}$$

where $W_{\alpha\beta}$ is the viscous correction to the ideal energy-momentum tensor. The "$\pm$" sign accounts for both contribution directions (increase and decrease) to the distribution function at a second order correction in viscosity. The inclusion of δf in hydrodynamical calculations has the effect of increasing particle spectra as a function of p_T because of the momentum dependence $\delta f \propto p^2$. This choice of momentum dependence is not unique [10, 81].

To evaluate the right hand side of the Cooper-Frye formula, Eq.(2.41), expressions for $u^\mu p_\mu$ and $p^\mu d^3\Sigma_\mu$ need to be determined. In a general, orthogonal coordinate system an infinitesimal element of the hypersurface is given by

$$d^3\Sigma_\mu = -\epsilon_{\mu\nu\lambda\rho} \frac{\partial\Sigma^\nu}{\partial u} \frac{\partial\Sigma^\lambda}{\partial v} \frac{\partial\Sigma^\rho}{\partial w} \, du \, dv \, dw, \tag{2.44}$$

where u, v, w are orthogonal coordinates which span the space, all indices run from 0 to 3, $\epsilon_{\mu\nu\lambda\rho}$ is the completely anti-symmetric Levi-Civita symbol in 4 dimensions, and the partial derivatives of Σ^ν are taken with respect to each spatial direction [80]. If longitudinal boost invariance is assumed it becomes convenient to use the $\tau - \eta$ coordinates, such that

$$\Sigma^\mu_f(x, y, \eta_s) = (\Sigma^\tau, \Sigma^x, \Sigma^y, \Sigma^{\eta_s}) = (\tau_f(x, y, \eta_s), x, y, \eta_s), \tag{2.45}$$

where $\tau_\mathrm{f}(x, y, \eta_s)$ is the complete proper time at freeze-out [9]. Taking the partial derivatives, one gets

$$d^3\Sigma_\mu = \Big(1, -\frac{\partial\tau_f}{\partial x}, -\frac{\partial\tau_f}{\partial y}, -\frac{\partial\tau_f}{\partial\eta_s}\Big) \sqrt{-\mathrm{detg}} \, dx \, dy \, d\eta_s, \tag{2.46}$$

$$= \Big(1, -\frac{\partial\tau_f}{\partial x}, -\frac{\partial\tau_f}{\partial y}, -\frac{\partial\tau_f}{\partial\eta_s}\Big) \tau_f \, dx \, dy \, d\eta_s, \tag{2.47}$$

where $g_{\mu\nu}$ is the metric in rapidity coordinates. The 4-momentum is given by a Lorentz

boosted expression of Equations (2.14)

$$p^{\tau} = m_T \cosh(y - \eta_s), \qquad p^{\eta_s} = \frac{m_T}{\tau} \sinh(y - \eta_s).$$

One can now write an expression for the two products

$$\begin{aligned} u^{\mu} p_{\mu} &= u^{\tau} p^{\tau} - u^{x} p^{x} - u^{y} p^{y} - \tau^2 u^{\eta_s} p^{\eta_s} \\ &= u^{\tau} m_T \cosh(y - \eta_s) - u^{x} p^{x} - u^{y} p^{y} - \tau u^{\eta_s} m_T \sinh(y - \eta_s), \end{aligned} \tag{2.48}$$

$$p^{\mu} d^3\Sigma_{\mu} = \left[m_T \frac{\partial}{\partial \eta_s} (\tau_f \sinh(y - \eta_s)) - \tau_f \vec{p_T} \cdot \vec{\Delta_T} \tau_f \right] dx\, dy\, d\eta_s, \tag{2.49}$$

where $\vec{\Delta_T}$ is the two-dimensional derivative in the transverse plane.

In hydrodynamical models, an algorithm based on a geometric approach is required to find the freeze-out hypersurface which, in most current programs, uses a trapezoidal surface method.

2.2.5 Resonance Decays

Resonances decay to lighter and more stable products and they are assumed to be produced at freeze-out along with their decay products. Resonances mostly decay into pions π, kaons K, and protons p. Hence the inclusion of resonance decays is expected to increase the particle yield of the lighter particles and their anti-particles. The final hadron spectra should include both direct thermal hadrons and the hadrons which are stable products of heavy resonances. The products of resonances are also assumed to freeze-out at T_{FO}. Different models include resonances below different cut-off masses. The hydrodynamical model developed in [6] includes resonances up to 1.68 GeV and MUSIC can include resonances up to 2 GeV. One can choose to include a smaller list of resonance particles. Both of these programs perform resonance decays from a generalized version of AZHYDRO [82, 83] which is extended to three spatial dimensions. The Results section of this work will compare computations with and without resonance decays to determine the significance of contributions from heavier unstable particles.

2.3 Initial Conditions of Heavy-Ion Collisions

The hydrodynamical evolution starts at a proper time τ_0 which is the estimated time for the system to have thermalized. Generally, this parameter is chosen to satisfy $\tau_0 \leq 1$ fm. Since tau_0 is an open parameter in heavy-ion collisions, we are free to chose a value for testing. Conventionally, a value of 0.4 fm for Au+Au collisions at RHIC energies has been chosen because it produces results which fit data quite well. Hence, the value of initial proper time used in this project is $\tau_0 = 0.4$ fm. However, it is expected that different values of τ_0 will change the details of the evolution and other choices of the initial proper time should be tested in the future.

The tube initial conditions refer to initial conditions which include only transverse fluctuations and event-by-event (E-by-E) initial conditions include both transverse and longitudinal fluctuations in what follows. It is very common to include fluctuations in the transverse direction. The fluctuations in the transverse direction correspond to different arrangements of partons in the heavy ions. Tube initial conditions correspond to a linear connection between partons from each heavy ion at the time of collision. Partons from different nuclei have a certain probability of interacting depending on a tight condition imposed on the distance between their centers. Tube initial conditions have a large energy density plateau in the η_s direction since the profile is flat for central values of η_s. In E-by-E initial conditions, partons which are not linearly connected can interact with a certain probability. There is a cut-off distance of interaction in E-by-E initial conditions but this is chosen to be much larger than for tube initial conditions. Fluctuations in the η_s (i.e. the longitudinal direction) is less commonly studied.

In Fig. 2.2, a plot of average energy density in units of fm^{-4} is given as a function of η_s. These energy densities are at the middle of the transverse plane, namely $x = y = 0$. We see that for the tube initial conditions the energy density is flat around $\eta_s = 0$. A completely boost invariant energy profile would consist of a flat energy density profile for all η_s but this is nonphysical since it would imply the system has an infinite amount of energy. Hence, the

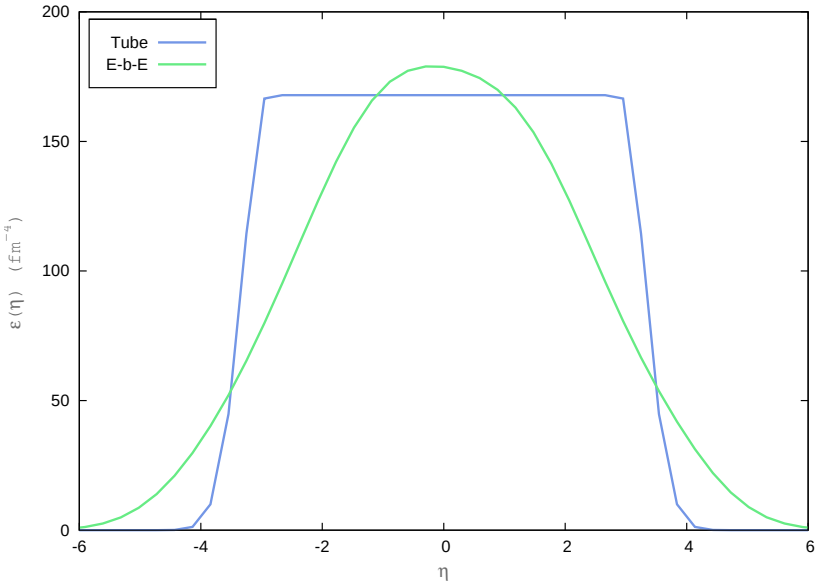

Figure 2.2: Initial energy density averaged over 100 events for 30-40% centrality bin with tube and E-by-E initial conditions.

tube initial conditions must eventually fall off smoothly to zero. This is usually done after a few units of spatial rapidity from the origin. The function used to describe the fall off is the product of a Gaussian and step function around $\eta_s = 0$ given as follows [9]

$$H(\eta_s) = \exp\Big[-\frac{(|\eta_s| - \eta_{\text{flat}}/2)^2}{2\sigma_{\eta_s}^2}\theta(|\eta_s| - \eta_{\text{flat}}/2)\Big]. \tag{2.50}$$

The variable η_s is the spatial rapidity defined by $\eta_s = \frac{1}{2}\ln\frac{t+z}{t-z}$ (it is important to make this distinction since there is also a momentum pseudo-rapidity variable η used in the results of MUSIC). Generally the initial conditions are given in terms of η_s since this variable easily maps to the usual space-time coordinates (x, y, z) and results are given as a function of η since this is the variable traced by experiments. The parameters η_{flat} and σ_η are fitted to data. The tube initial conditions provided by AMPT contain all required information on the plateau and fall-off of the profiles. The full initial energy density at the initial proper time τ_0 and as a function of impact parameter b is given by [9]

$$\epsilon(x, y, \eta_s, b) = \epsilon_0 H(\eta_s) W(x, y, b)/W(0, 0, 0). \tag{2.51}$$

The function $H(\eta_s)$ gives us the longitudinal profile of the tube initial conditions and $W(x, y, b)$ and its normalization $W(0, 0, 0)$ give us the transverse fluctuations and its normalization respectively. The constant ϵ_0 is the overall scaling factor of the energy density. The function $W(x, y, b)$ depends on the initial conditions. For example, one can use the Glauber model to obtain the transverse distribution of density as a function of the transverse coordinates and the impact parameter. The normalization $W(0, 0, 0)$ is the transverse distribution function at the origin of the transverse plane for an $b = 0$ collision. AMPT provides the initial profile $\epsilon(x, y, \eta_s, b)$. Since the system is sensitive to the choice of initial conditions, equation of state, and several parameters of the system, the analysis is not always simple. However, the use of more realistic initial conditions is one of the strongest inputs in a hydrodynamical model.

2.3.1 AMPT Model for Hydrodynamic Initial Conditions

The AMPT model is a multi-phase transport model. It is coined multi-phase because it is a hybrid model consisting of 4 components: the initial conditions, partonic interactions, the conversion from partonic to hadronic matter, and hadronic interactions [5]. The initial conditions are computed using the HIJING model [84] and the ZPC model [85] takes the initial conditions produced by HIJING to treat the partonic interactions until the hadronic phase starts. At this point, either the Lund string fragmentation model [86] or a quark coalescence model is used to convert the partons into hadrons. The AMPT version used in this project is ampt-v1.26t1-v2.26t1 with the string melting option from 2008 and is found on the OSCAR website [87]. Table A.2 provides a list of input parameter choices in the AMPT model.

Only the first two components of the AMPT model are of interest here (the initial conditions and partonic interactions). This is because MUSIC will take as input the final result of the partonic interactions as initial conditions for its runs, where the partons will evolve

hydrodynamically after they have thermalized and the phase transition from partonic to hadronic matter will take place as the medium cools. AMPT on the other hand, treats the hadronic evolution using a relativistic transport model [5]. What is of importance here is that AMPT will treat all of the geometry and dynamics which occur before thermalization at τ_0.

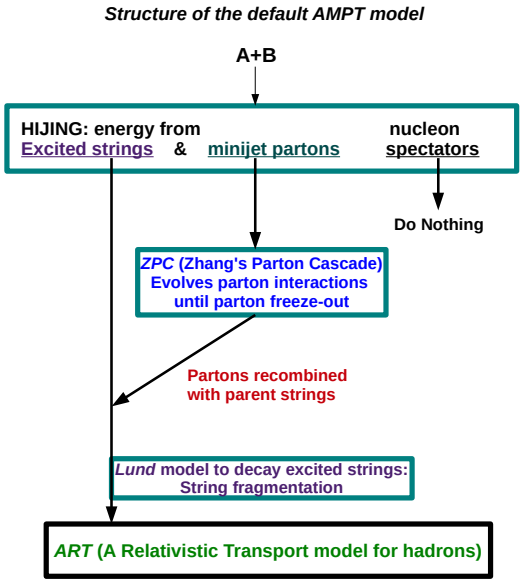

Figure 2.3: Schematic illustration of the default AMPT model for $A + B$ nuclear collisions. Time evolution is from top to bottom.

There are two versions of the AMPT model: The AMPT which does not include string melting (default AMPT model) [88, 89, 90] and the model which includes strong melting (string melting AMPT model) [91, 92, 93]. Present in all current versions of AMPT, the parameter $ISOFT$ sets the model to run with or without string melting. If string melting is included, one can choose which type of particle decompositions to include. Table A.2 in the Appendices shows the string melting version was used for the results in this project ($ISOFT = 4$). The AMPT model is written in Fortran 77 and is available online on the OSCAR and EPAPS websites [5]. Fig. 2.3 illustrates the structure of the default AMPT model and Fig. 2.4 illustrates the AMPT model with string melting [5, 6, 91, 92, 93]. The second option is of relevance here. The following two sections will discuss the HIJING and ZPC models, which together are used to compute the thermalized $T^{\mu\nu}$ in AMPT.

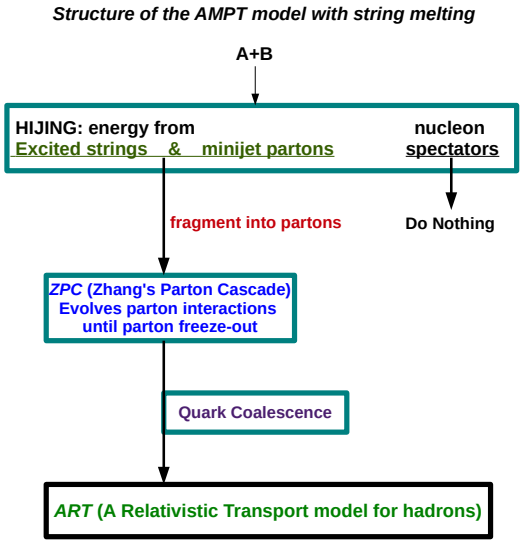

Figure 2.4: Schematic illustration of the AMPT model which includes string melting for $A + B$ nuclear collisions. Time evolution is from top to bottom.

HIJING Model: Initial Conditions for AMPT Model

The AMPT model uses the HIJING model to produce its initial conditions. The HIJING model is a Monte-Carlo model which treats phenomenological problems evident in nuclear collisions such as nuclear (parton) shadowing, multiple mini-jet production, and jet quenching in dense matter [84]. HIJING incorporates the pQCD approach to multiple jet processes which also treat jet quenching and nuclear effects in the medium. Hence, HIJING treats the non-perturbative low-p_T processes (soft sector), multiple mini-jet production, and also the rare high-p_T processes (hard sector). The spectator nucleons are directly included into the hadron evolution program ART as depicted in Fig. 2.3 and 2.4.

The initial geometry of the AMPT model, the number of participants, and the number of nucleon-nucleon collisions are determined with the Monte-Carlo Glauber model. The Glauber model is based on a Wood-Saxon nuclear distribution and determines the number of partons which collide based on the initial geometric transverse profile of nuclei before collision time. The Glauber model parameters and formulae are explained in more detail in Section 2.4.

The HIJING model treats the low-p_T processes via excited strings and high energy pro-

cesses via mini-jet partons. Since the number of hard collisions roughly scales as $A^{4/3}$, where A is the number of participating nucleons (and grows quickly with colliding energy), and the number of strings scales as the number of participant nucleons A, minijet production becomes increasingly important when the energy of heavy ion collisions increases [84]. In particular, the number of mini-jets per binary nucleon-nucleon collision follows a Poisson distribution with an average given by the mini-jet cross-section [6].

Another important nuclear process included in HIJING is nuclear shadowing [94, 95]. Nuclear shadowing is an important effect when a nucleus collides with a proton or another nucleus. The reason for this is that the nucleon collisions are affected by the presence of other nucleons in the vicinity of the collision, and this effect shifts the momentum of the quarks and gluons. This shift in momentum changes the probability of any quark-quark, gluon-gluon, and quark-gluon interaction. This change to the parton distribution functions (PDFs) is included in HIJING and other models as a parametrization [96]. In the HIJING model, this effect is included via an impact parameter dependent, but Q^2 and flavor independent, parametrization of the parton distribution function f_a [5]

$$\begin{aligned} R_A(x,r) &\equiv \frac{f_a^A(x,Q^2,r)}{A f_a^N(x,Q^2)} \\ &= 1 + 1.37\,(\log A)^{1/6}(x^3 - 1.2x^2 + 0.21x) \\ &- \left[\alpha_A(r) - \frac{0.47(A^{1/3}-1)\sqrt{x}}{\log(A+1)}\right] e^{-x^2/0.01}, \end{aligned} \tag{2.52}$$

where x is the light-cone momentum fraction of parton a, r is the transverse distance of an interacting nucleon from the center of the nucleus, and the nucleus radius is given by R_A. The impact parameter dependence of the nuclear shadowing effect is defined as $\alpha_A(x)$

$$\alpha_A(r) = 0.133(A^{1/3}-1)\sqrt{1 - r^2/R_A^2}. \tag{2.53}$$

The string melting mechanism takes all excited strings (i.e. unstable due to energy departed to them at initialization) which are not spectator nucleons and converts them into

partons according to the flavor and spin structures of their valence quarks. In particular, a meson is converted into a quark and anti-quark, while a baryon is first converted to a quark and di-quark, then the di-quark is decomposed into two quarks. The mesons and baryons do not exist in the initial conditions but are created in the AMPT algorithm.

All of the above two-body decompositions are isotropic in the rest frame of the parent hadron or di-quark. The resulting partons are not allowed to scatter before an estimated formation time $t_f = E_H/m_{T,H}^2$ where E_H and $m_{T,H}$ are the energy and transverse energy of the parent hadron. It is introduced as the production time of the partons from strong color fields and depends on the momentum of the hadron. Imposing a momentum-dependent delay in time also ensures that partons from the same parent hadron have the same formation time. The advantage of this choice in the string melting mechanism is that the AMPT model (without considering the interactions) is the same as the HIJING model. In the HIJING model, and hence also in the initial conditions of AMPT with string melting, the partons with the same formation time will find each other as closest partners at partonic freeze-out and coalesce back to the original hadrons. To compute the initial positions of partons from melted strings, straight line trajectories of the parent hadron positions are used. The partonic interactions are evolved in the ZPC program as described below.

ZPC Model: Partonic Interactions

The parton interactions are treated with the transport model approach with the equations of motion of their Wigner distribution function [5]. These functions semi-classically describe the density of partons in phase space. Since the model only treats two-body scattering the Boltzmann equations, for each parton a and distribution function $f_a(\vec{x}, \vec{p_1}, t)$, take the form

$$\begin{aligned} p^\mu \partial_\mu f_a(\vec{x}, \vec{p_1}, t) = C \sum_{b,c,d} \int \frac{d^3p_2}{(2\pi)^3 2E_2} \frac{d^3p_3}{(2\pi)^3 2E_3} \frac{d^3p_4}{(2\pi)^3 2E_4} \times |M_{12\leftrightarrow 34}|^2 \\ \times (f_b(p_3) f_c(p_4) - f_a(p_1) f_d(p_2)) \\ \times (2\pi)^4 \delta^4(p_1 + p_2 - p_3 - p_4), \end{aligned} \tag{2.54}$$

where C is the energy factor for the different parton species a, b, c, d, $|M_{12\leftrightarrow 34}|$ is the two-body partonic scattering matrix element (which also depends on parton species), and $f_b(\vec{x},\vec{p_3},t)$, $f_c(\vec{x},\vec{p_4},t)$, $f_d(\vec{x},\vec{p_4},t)$ are the distribution functions of the respective partons. The delta-function ensures conservation of energy-momentum. The Boltzmann equation is solved using Zhang's parton cascade (ZPC) which allows two partons (from mini-jets or string fragmentation) to interact if they approach a distance within $\sqrt{\sigma/\pi}$. The partonic cross-section σ used in this model is calculated using pQCD and takes the form

$$\sigma_{pp} \approx \frac{9\pi\alpha_s}{2\mu^2}, \tag{2.55}$$

where α_s is the strong coupling constant, μ is the screening mass generated as a result of calculating interactions in a dense medium. The above cross-section only includes leading divergent terms, and the approximation $s > \mu^2$, which holds in hot QGP, is taken. The different cross-sections can be obtained by changing the value of the screening mass. For the elastic interaction of gluons, a screening mass of 3 fm^{-1} yields an approximate cross-section of 3 mb. This cross-section is used in both the default and string melting AMPT models. The Casimir factors for quarks and gluons have been neglected in the cross-section for simplicity.

Fluctuations and $T^{\mu\nu}$ in the AMPT model

The results of the AMPT model contain two important effects which have not previously been studied in detail. First, since initial conditions are not boost invariant, the energy densities vary in the longitudinal direction as well as in the transverse directions (E-by-E). In the longitudinal direction, the profile is non-trivial and hence produces flow effects which are closer to actual experiments. All initial conditions studied here will include transverse fluctuations.

In transverse fluctuating initial conditions, there are some regions which will be dense with nucleon collisions and some which will be more dilute. This is due to the random initial positioning of the nucleons and their collisions. The dense collision regions are termed hot

spots and cold valleys are the more dilute regions. The presence of these highly non-symmetric profiles makes for a very anisotropic local pressure gradient. Hence, the flow is expected to be highly non-symmetric resulting in larger odd flow coefficients. When several E-by-E events are averaged, the profile becomes increasingly symmetric in the transverse plane and it is therefore expected that even flow coefficients (such as elliptic flow) will increase and odd flow harmonics will decrease as a result of this averaging. In standard hydrodynamic simulations, the limit of many averaged initial conditions is taken and in this limit all of the odd harmonics vanish [10]. By definition, the fluctuations in the transverse plane generate all flow harmonics as a result of the initial anisotropic geometry.

In addition to the inclusion of longitudinal fluctuations, AMPT also includes non-zero initial spatial flow. This is a relatively new feature which can be included in hydrodynamical calculations. Recent E-by-E hydrodynamical simulations have mostly assumed zero local flow velocities. Those studies which have included initial local flow have not systematically studied the effects [6]. It is important to include initial local flow if one also includes fluctuations of the order of the nucleon size $n_{\rm size}$ or less. If fluctuations were smoothed over a transverse area $A_{\rm trans} \gg n_{\rm size}$ it can be assumed that the initially produced partons from mini-jets will be uncorrelated in different nucleon-nucleon collisions at the edge of a large area $A_{\rm trans}$. However, when fluctuations are the size of the nucleon or less, correlations between partons associated with a pair of mini-jets are not necessarily destroyed at the initial proper time τ_0, leading to non-vanishing local flow velocities [97]. In a nutshell, if there are many correlated partons, these correlations can survive until the hydrodynamic evolution begins, and fluctuations in the profile are comparable to nucleon size than the initial local flow should be included in the simulations. Fig. 2.5 shows the initial local flow velocity profile of a typical AMPT event in the transverse plane.

The space-time positions of the created partons are recorded at the last scattering or formation time. Most partons are concentrated along the hyperbola of the initial time τ_0 [5], and evolve in lines of constant proper time. Hence, the proper time τ_0 is assigned to

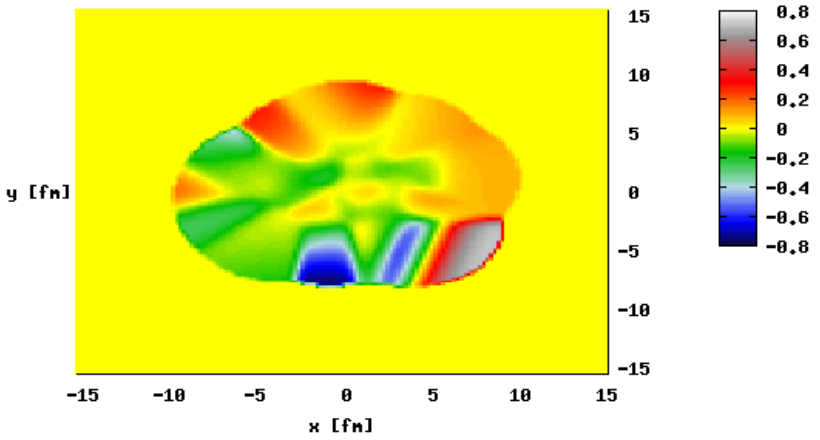

Figure 2.5: Initial transverse velocity profile $u_y(x, y)$ for a typical AMPT event. Generally, the flow is away from the origin. Flow can locally change due to the presence of hot spots, cold valleys, and jets.

all partons as an approximation, and the parton 4-momenta is used to compute the energy-momentum tensor $T^{\mu\nu}$. This approximation is a first step one can take and it should be revisited for future improvement.

Taking the 4-momenta to compute the energy-momentum tensor and approximating the value of $T^{\mu\nu}$ as a Gaussian distribution in each cell, one ansatz for the form of $T^{\mu\nu}$, in rapidity coordinates, is

$$T^{\mu\nu}(\tau_0, x, y, \eta_s) = K \sum_i \frac{p_i^\mu \, p_i^\nu}{p_i^\tau} \frac{1}{\sqrt{2\,\pi\,\sigma_{\eta_s}^2}} \frac{1}{2\,\pi\,\sigma_r^2} \times \exp\left[- \frac{(x - x_i)^2 + (y - y_i)^2}{2\,\sigma_r^2} - \frac{(\eta_s - \eta_{is})^2}{2\,\sigma_{\eta_s}^2} \right], \tag{2.56}$$

where $p_i^\tau = m_{iT} \cosh(y_i - \eta_{is})$, $p_i^x = p_{ix}$, $p_i^y = p_{iy}$, $p_i^\eta = m_{iT} \sinh(y_i - \eta_{is})/\tau_0$, and the sum i runs over all partons produced in the AMPT simulation. The momentum-rapidity for particle i is given by y_i (defined in Eq.(2.13)) and η_{is} is the spatial rapidity for particle i. It is common to approximate $T^{\mu\nu}$ as a Gaussian in the transverse plane, one should note that a Gaussian smearing is also taken in the spatial rapidity direction in the above approximation. In this project, the width parameters have been set to the following values, $\sigma_r = 0.6$ fm and $\sigma_{\eta_s} = 0.6$ to compare to results in [6]. The transverse energy m_T, the spatial pseudo-rapidity η_s, and the rapidity y are calculated from each parton's 4-momentum and spatial coordinates.

The scale factor K, and the proper time τ_0 are the two parameters which can be used to fit

Description	K	τ_0 (fm)
Ref. [6] at RHIC energies, $\sqrt{s_{\rm NN}} = 200$ GeV, Au+Au	1.45	0.4
Ref. [6] at LHC energies, $\sqrt{s_{\rm NN}} = 2.76$ TeV, $Pb + Pb$	1.6	0.2
Thesis at RHIC energies, $\sqrt{s_{\rm NN}} = 200$ GeV, Au+Au	1	0.4

Table 2.2: $T^{\mu\nu}$ fitting parameters (τ_0 and K) used by stated reference and those used for this project.

experimental data. Table 2.2 shows the parameters used in Reference [6] and the parameters used in this project. It is believed that taking a scaling factor K which is not unity will not correspond to the chosen EOS. Hence, $K = 1$ was taken in this project.

2.4 Monte Carlo Glauber Model: Initial Geometry

The Glauber model was developed to address the problem of composite-particle collisions at high energies. The Glauber model (Optical and Monte Carlo models) are based on the use of quantum-mechanical scattering theory for non-trivial systems of composite particles such as $p + A$ and $A + B$ collisions [1]. In this project, the Monte Carlo Glauber model was used to determine the initial positions of nucleons within AMPT before the hydrodynamical evolution. In this model, the nucleus is treated as a sum of uncorrelated nucleons whose positions are sampled from measured density distributions. The nucleons are assumed to be traveling along a straight longitudinal trajectory. The measured density distribution of the nuclei resembles very closely the Woods-Saxon parametrization

$$\rho_A(r) = \frac{\rho_0}{1 + \exp[(r - R)/a]}, \tag{2.57}$$

where R is the nucleus radius and a measures the diffuseness of the density. The normalization factor ρ_0 is set to satisfy the total charge density of the nucleus when integrated over its entire volume: $\int d^3x \rho_A(r) = A$. For Au nuclei, $R = 6.38$ fm and $a = 0.535$ fm. With these values the normalization factor is $\rho_0 = 0.17$ fm^{-3}, where $r = \sqrt{x^2 + y^2 + z^2}$ and is measured in low-energy electron scattering experiments [1, 9, 98].

The Wood-Saxon distribution determines the positions of the nucleons but the model also needs a method for estimating the number of binary collisions. This is done by defining a thickness function in the transverse plane for each nucleus

$$T_A(x,y) = \int_{-\infty}^{\infty} dz \rho_A(x,y,z). \tag{2.58}$$

With the thickness function, the number density of binary collisions is determined by taking the product of each nucleus' thickness function and the total inelastic cross-section σ_0 of the nucleus-nucleus collision

$$n_{BC}(x,y,b) = \sigma_0 T_A(x+b/2,y) T_B(x-b/2,y). \tag{2.59}$$

The number density of binary collisions n_{BC} considers the possibility of multiple (hard) scatterings of nucleons and is a function of impact parameter. The total number of binary collisions is given by integrating n_{BC} in the transverse plane [4]. Another important consideration is to determine if any two nucleons are considered to interact. Since the nucleons are modeled by Gaussians, the Gaussian tails of nucleons which are physically far away from each other will have a certain probability of interacting. However, for practicality, a distance condition is put in by-hand so if the centroids of nucleons lie within a distance [11]

$$d \leq \sqrt{\frac{\sigma_{\text{inelastic}}}{\pi}} \tag{2.60}$$

in the transverse plane they are considered to have collided. Otherwise, the collision is omitted and is not allowed to occur numerically. The following subsection briefly outlines the steps taken in the Monte-Carlo Glauber model used to extract the centrality bin correspondence for 5% centrality bins.

Chapter 3

Procedure

A description of the steps taken to produce the numerical simulations will be explained in this chapter. This involves explaining some of the most important input parameters in MUSIC and AMPT along with other specifications.

3.1 Input Parameters

It is important to use a fine grid in (x, y, η_s) because it improves the calculations of higher harmonic flow coefficients such as v_4. Another advantage of using a finer gird is in using the KT scheme where numerical viscosity is seen to decrease with finer lattice size [9]. Computation time has to also be taken into consideration because a finer grid will require longer run time and hence be more computationally expensive. The results in article [9] use $\Delta x = \Delta y = 0.3$ fm and $\Delta\eta_s = 0.3$. In this project, a finer grid was used to make comparisons to another group's results. However, if the energy density is large (or if it expands quickly such as in the ideal hydrodynamical runs) a larger grid is needed. Table 3.1 shows the grid size and number of cells used along with the associated Δx, Δy, and $\Delta\eta_s$.

Result Section	(x, y) Grid size [fm]	η_s Grid size	Number of grid points (x, y)	Number of grid points η_s	(Δx, Δy) [fm]	$\Delta\eta_s$
Section 4: 30-40%	(30.8, 30.8)	19.2	(144, 144)	65	(0.2, 0.2)	0.3

Table 3.1: Record of the spatial grid sizes. Computation time should be considered when choosing the number of grid points.

Resonance Decays	Mass Correction (GeV)	Spectra Diff. (%)
π^+ to n^- (1440)	1.44	27
K_1 (1270) to n^- (1440)	0.17	3
$\overline{K_1}$ (1400) to n^- (1440)	0.04	1

Table 3.2: Summary of the difference of results shown in Fig. 3.1 are numerically given for pi^+ spectra.

In practice, it is also computationally expensive to include all resonances up to 2 GeV, especially if thousands of events are computed. Hence, only resonances up to and including 1.44 GeV (i.e. n^- (1440)) are included. This particle corresponds to the 100^{th} lightest particle given in the Particle Data Group [99]. Fig. 3.1 shows the difference between including resonance decay particles up to 1.44 GeV, 1.40 GeV (80^{th} lightest particle i.e. $\overline{K_1}$ (1400)), 1.27 GeV (50^{th} lightest particle, i.e. K_1 (1270)), and including no resonance decays. The correction of going from including no resonance decays to resonances up to 1.44 GeV is 27%. While the correction of going from 1.27 GeV to 1.44 GeV is an 3%, and from 1.40 GeV to 1.44 GeV is only an 1% correction. Therefore, one can expect that including resonances heavier than 1.44 GeV will contribute a very small correction to the calculations. The reason for this is that heavier particles require more energy to be created and hence they are rarely found—even in the most energetic collisions.

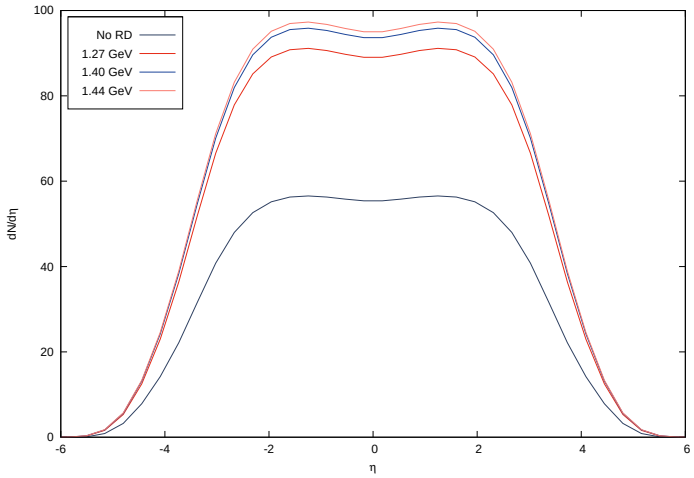

Figure 3.1: Spectra $dN/d\eta$ for π^+ is shown for different resonance decay inclusions. The masses quoted in the key is the heaviest particle included for the presented calculation. The set of tube initial conditions and viscous hydrodynamics is shown for demonstration purposes.

The parton data was used to produce $T^{\mu\nu}(\tau_0, x, y, \eta)$ from the AMPT model. This data

was used to initialize MUSIC, and the hadronic freeze-out in MUSIC was chosen to be $T_{\rm FO} = 0.137$ GeV—to make comparisons to results provided by another group's hydrodynamical runs possible. A summary of the computational stages taken to arrive at the final observables are given in Fig. 1.1.

Each event was run with a centrality value randomly chosen from the range of impact parameters provided for every bin class. To produce tube initial conditions, an E-by-E initial energy density profile was taken and the central most cells in η_s were averaged in energy density. The average central energy density value (defined at each point in the transverse plane) was used to produce a tube profile in the η_s-direction using Eq.(2.50). This equation produces a tube envelope profile with a maximum value taken to be the average of the central η_s cells in the corresponding E-by-E event. It is also possible to produce tube initial conditions by averaging many E-by-E events. This should be done in the future for comparison

3.2 Monte Carlo Glauber Model for Centrality bins

The impact parameter bin for 30%-40% was computed and provided by another group using the Monte Carlo Glauber (MCG) model [6]. There are some distinctions between MCG and the optical limit which depend on the particular context. The optical limit is modeled with the Optical Glauber (OG) model. Both models consider the individual interactions between nucleons. At high energies, the OG model assumes that the nucleons carry enough momentum so that they are not deflected as the nuclei pass through each other. This approximation allows one to write simple analytic expressions for the interactions which take place at the nucleon level with the nucleon-nucleon cross-section. Also, the model assumes that the incoming nucleons see the target nucleons as a smooth distribution [1]. This approach captures many aspects of the collision but does not capture important physics involved in the total nucleus cross-section. The presence of many nucleons surrounding a collision creates a shadowing effect on any one nucleon-nucleon collision. The MCG model albeit simple, captures

the shadowing effects of the collisions. The inclusion of shadowing effects reduces the total cross-section compared to results given by the OG model. The main difference between the two models occurs at high impact parameters [1] as shown in Fig. 3.2.

In order to compute the centrality range values, the MCG model was run for 500 000 events [1]. The program first defines the cross-section of nucleon-nucleon collisions, σ, which is a function of collision energy and is estimated theoretically using experimental data [1]. This will be used to determine the probability that a collision occurs. In this case a RHIC energy of $\sqrt{s_{\mathrm{NN}}} = 200$ GeV is used. Next, the program finds the position of the nucleons (in each nucleus) using the Wood-Saxon distribution discussed above. Finally, the collisions are performed and the position and number of binary collisions is recorded. From these results, the number of participants can also be computed. The number of participants is simply the sum of the nucleons which collided with a given cross-section.

After the program is done, the events are organized in terms of decreasing number of participants since the more central events have more participants. The output of this program for each event is the event number, number of participants, number of binary collisions, and the impact parameter range (given by OG) or average (given MCG). Since the MCG model only provides average impact parameter values, the impact parameters were computed for each 1% centrality bin so any bin class size can be calculated from these centrality values. The MCG model was used for simplicity and to capture nuclear shadowing effects which are also included in the AMPT model [5].

Since the number of participants was shown to decrease linearly with impact parameter (for example, see Fig. 8 of reference [1] and Ref. [101]), the total number of organized events was divided by the number of events in each 5% bin to obtain the range of impact parameters, b_{min} and b_{max} for each centrality class. From here, the average impact parameter was computed for each bin class. The impact parameters follow the following pattern $[0, b_{\mathrm{max1}}]$, $[b_{\mathrm{max1}} = b_{\mathrm{min2}}, b_{\mathrm{max2}}]$, $[b_{\mathrm{max2}} = b_{\mathrm{min3}}, b_{\mathrm{max3}}]$, and so on. Table 3.3 shows the results of this

[1] It was checked that using more events improves results only slightly.

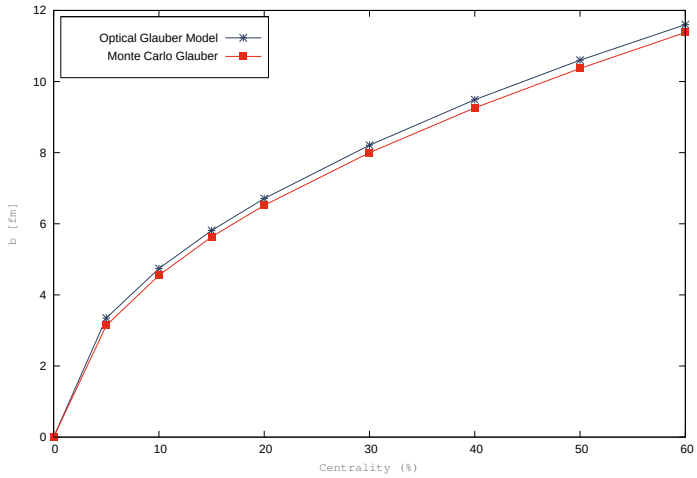

Figure 3.2: Comparison between centrality values using the Monte Carlo and Optical Glauber models. Optical Glauber model results were published in [100].

Range (%)	0-5	5-10	10-15	15-20	20-25	25-30	30-35	35-40	40-45	45-50	50-55	55-60	60-65	65-70
b_{min}	0	3.14	4.55	5.63	6.52	7.31	8.00	8.66	9.26	9.83	10.37	10.89	11.38	11.86
b_{max}	3.14	4.55	5.63	6.52	7.31	8.00	8.66	9.26	9.83	10.37	10.89	11.38	11.86	12.33
$\langle b \rangle$	1.57	3.85	5.09	6.08	6.92	7.66	8.33	8.96	9.55	10.1	10.63	11.14	11.62	12.1

Table 3.3: Centrality bins produced using the Monte Carlo Glauber model for Au+Au at $\sqrt{s_{\text{NN}}} = 200$ GeV. Average impact parameter for each centrality class is also shown.

program.

These results were compared to published data in [100] using the OG model, and they compared well. A comparison between the two results is shown in Fig. 3.2. It is worth noting that the ideal approach to determining the centrality classes is to use the AMPT model to compute impact parameter classes. This is the most consistent approach since the pre-thermalization process is computed from the AMPT model. However, the Glauber model is commonly used for most works (including by the AMPT group, see [6] for example), hence this is the approach also used in this project and is used in all RHIC experiments [1].

Chapter 4

Results and Analysis

All of the results in this thesis are for Au+Au collisions at RHIC energies of $\sqrt{s_{\rm NN}} = 200$ GeV at 30-40% centrality, and all results include resonance decays (RD) unless stated otherwise. The viscous correction δf was turned on for all the results which will be presented here. Also, the shear viscosity was turned on (with $\eta/s = 1/4\pi$ as quoted in Table A.1) where specified. Results presented include both tube and E-by-E initial conditions. As described previously, tube initial conditions include transverse fluctuations but are boost invariant in the longitudinal direction. E-by-E initial conditions include both transverse and longitudinal fluctuations. All initial conditions include initial local flow fluctuations. The average of 100 events was taken for each plot. Finally, results include resonance decay products unless stated otherwise. The purpose of these results is to study a variety of different observables from a hydrodynamical model for Au+Au collisions at RHIC energies. Comparisons of results will be done with results from another group (which will be referred to as AMPT results [6]) and to data where possible. The comparisons to AMPT results is only done for ideal hydrodynamics since viscous hydrodynamics by [6] or other groups has not been computed up to date. Hence, since this is the first work to include AMPT initial conditions and viscous hydrodynamics, comparisons to other groups are only meaningful if they are computed with ideal hydrodynamics.

	Multiplicity
Tube + ideal hydro	1663
Tube + viscous hydro	2089
E-by-E + ideal hydro	1727
E-by-E + viscous hydro	2158

Table 4.1: The total average multiplicity $N_{\rm ch}$ of charged particles for both sets of initial conditions and for ideal and viscous hydrodynamic results.

4.1 Spectra

Comparisons between tube and E-by-E initial conditions will be done on grounds that their total multiplicities are roughly equal. The total average multiplicity of charged hadrons with resonance decays included in the calculation are listed in Table 4.1. The ideal hydrodynamic runs should be compared with each other and similarly for the viscous runs. The average multiplicities in Tables 4.1 and 4.2 are computed by summing over pseudo-rapidity for the entire computation range $-8 < |\eta| < 8$, integrating particles of all momenta, and including resonance decay contributions. This range was chosen to make comparisons to another group's results possible. All of the observables shown give one an idea of the different distributions of data and are measurable quantities.

The multiplicities in viscous hydrodynamics is expected to be larger than the ideal case since entropy increase due to viscosity will result in higher particle yield. From Table 4.1 it can be concluded that this is indeed the case. Also shown in Fig. 4.1, the viscous correction for total charged particle multiplicity is approximately an 25% increase from its ideal counterpart. The AMPT results for total multiplicity were computed by interpolating the given $dN/d\eta$ results than integrating numerically over the entire pseudo-rapidity range. Fig. 4.2 shows spectra results for π^+ from MUSIC simulations with and without resonance decays. Results are also shown from another group who ran the same AMPT initial conditions with a different hydrodynamical model. The results provided by AMPT group do not provide resonance decays and they compare well with corresponding results from MUSIC and only differ by roughly 10%.

The charged hadron calculations in this section include $\pi^{\pm}$, $K^{\pm}$, and $p^{\pm}$. Heavier charged

	Multiplicity π^+
MUSIC with RD	
Tube + ideal hydro	685
Tube + viscous hydro	859
E-by-E + ideal hydro	713
E-by-E + viscous hydro	890
MUSIC without RD	
Tube + ideal hydro	294
Tube + viscous hydro	394
E-by-E + ideal hydro	311
E-by-E + viscous hydro	435
AMPT	
Tube + ideal hydro	341
E-by-E + ideal hydro	359

Table 4.2: The total averaged multiplicity of π^+ for both sets of initial conditions with a comparison to AMPT results.

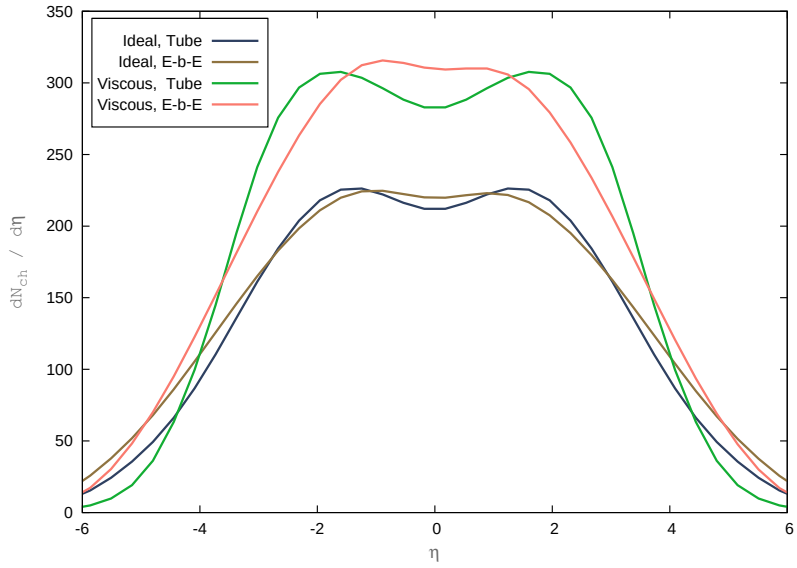

Figure 4.1: $dN/d\eta$ spectra as a function of η is shown for charged hadrons. Both sets of initial conditions (E-by-E and tube) and both sets of hydrodynamics (ideal and viscous) are shown.

hadrons only slightly change this sum. The percentage difference for the p^+ contribution to the lighter products is already only an 1% correction as can be seen in Fig. 4.3, hence heavier particles than the proton would contribute an even smaller correction to the total spectra sum.

In Fig. 4.2, the correction in MUSIC results due to including resonance decays up to 1.38 GeV is significant since it is approximately a 30% correction. This is because the initial

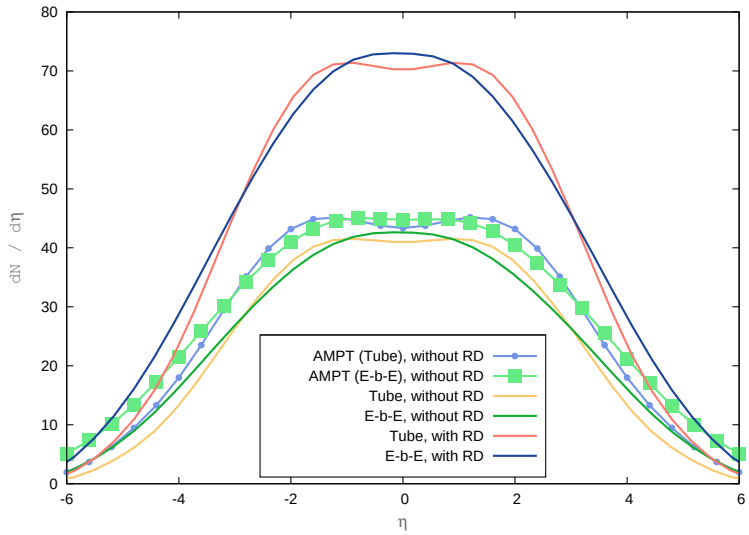

Figure 4.2: $dN/d\eta$ spectra for π^+ from MUSIC (with and without the inclusion of resonance decays) compared to another group's results. MUSIC results without resonance decays are to be compared to results from the AMPT group. Results from ideal hydrodynamics are shown.

energy of the collision is large and so the production of heavy particles is more probable. Again, results for spectra as a function of η are comparable between MUSIC and AMPT results. There is one more set of available data from AMPT which will be used as a comparison for $dN/p_T dp_T dy$ calculations later on in this analysis.

Fig. 4.3 shows the spectra as a function of momentum pseudo-rapidity for the charged particles π^+, K^+, and p^+. The yield for π^+ is the largest since this is the lightest stable particle. The viscous correction is about an 30% increase from the ideal hydrodynamic results due to the increase in entropy which results in the production of more particles. Also due to the slowing down of the flow velocity in viscous hydrodynamics, the particle spectra fall-off occurs closer to the center. This is because viscosity restricts flow of the medium. The double peak feature in $dN/d\eta(\eta)$ present in these results is also observed in data and models with other initial conditions such as those from the Glauber model [9, 12].

It is expected that the same number of π^+ and π^- will be produced in heavy-ion collision models based on charge symmetry. Experimentally, π^0 is harder to measure because it is chargeless, however it is expected to have different spectra results from $\pi^\pm$ due to its different mass. In hydrodynamical models, the equation which determines the production of

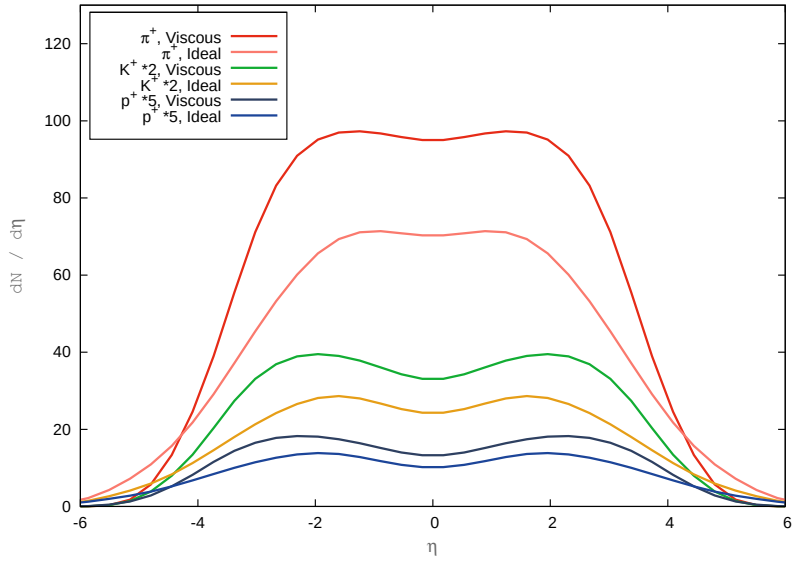

Figure 4.3: Spectra for identified charged hadrons with tube initial conditions. Ideal hydrodynamical results are presented.

these particles is the Cooper-Frye formula. This formula takes into consideration the mass and degeneracy. Since m_{π^0} is only slightly different from $m_{\pi^\pm}$ and has unit degeneracy, it is expected that the results of π^0 are comparable to those of $\pi^\pm$. Regarding $K^\pm$, these particles are expected to have the same spectra since the strangeness of the initial nuclei is zero. Hence, the appearance of strange and anti-strange quarks cancels. Finally, for p^+ and p^-, due to an initial non-zero baryon number, one expects to see more final p^+ than p^- particles, and this is what is observed experimentally. The difference between these two spectra decreases for lighter nuclei because they have a smaller initial baryon number. However, since the initial baryon density is assumed to be zero, these spectra are expected to be exactly the same for particles and their anti-particle based on the structure of the Cooper-Frye formula.

Fig. 4.4 shows the $dN/d\eta$ spectra for ideal and viscous hydrodynamics. The double-peak behaviour in Fig. 4.4 is visible for K^+ and p^+ however it is not as clear in π^+ spectra. If this result is compared with Fig. 4.5—a comparison of spectra as a function of dynamic-rapidity and pseudo-rapidity for tube and E-by-E initial conditions—one concludes that the effect is the Jacobian effect of $d\eta/dy$.

The spectra for E-by-E events should be symmetric if a large enough sample is taken.

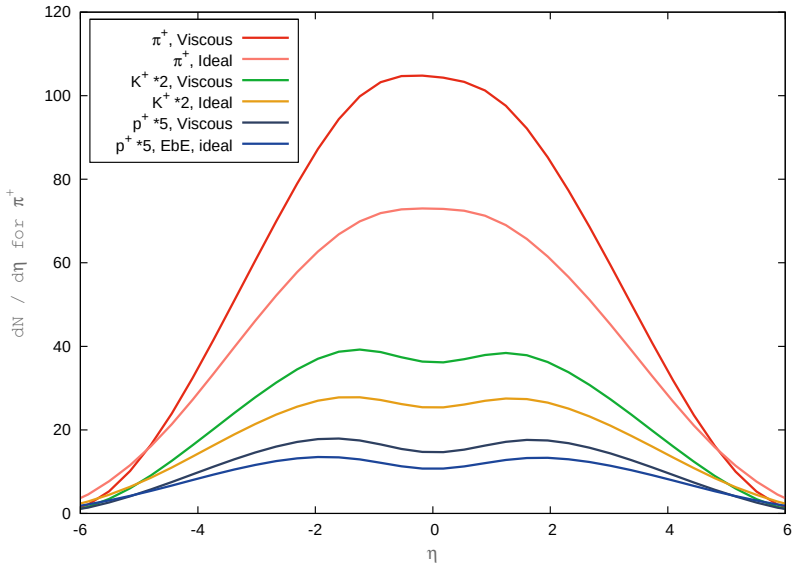

Figure 4.4: $dN/d\eta$ spectra for identified hadrons with E-by-E initial conditions. Hydrodynamic simulations with and without shear viscosity are included.

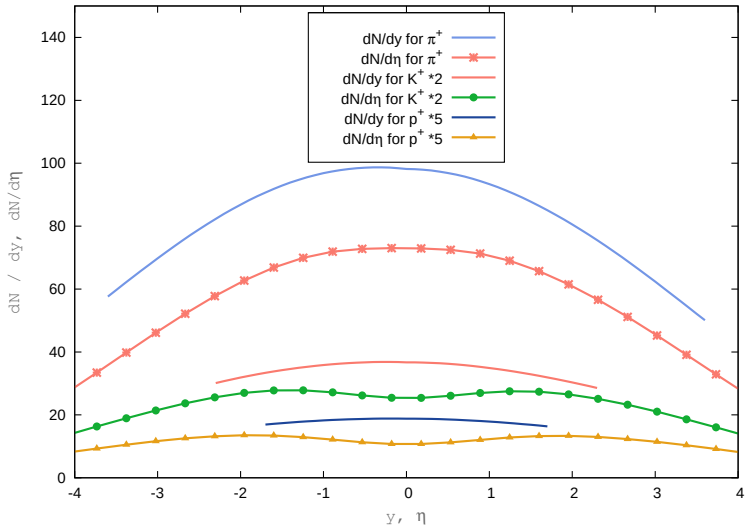

Figure 4.5: Comparison between dN/dy and $dN/d\eta$ spectra for identified hadrons is shown. Results are shown for E-by-E initial conditions and ideal hydrodynamics.

From the slight asymmetry observed in the E-by-E results in Fig. 4.4, we learn that the fluctuations provided by AMPT are fine and require a larger sample for averaging.

Fig. 4.6 shows p_T-spectra ($dN/p_T dp_T dy$) with comparisons to AMPT group results and PHENIX data. p_T-spectra values are given on a logarithmic scale. Fig. 4.6 also shows MUSIC results with and without resonance decays and MUSIC results quoted here are for

ideal hydrodynamics. Results for p_T spectra vary non-significantly from one set of initial conditions to another and are larger than data for high p_T values. This effect is expected since the presence of hot spots increases the high-p_T spectra due to increased local energy. Also, the inclusion of δf given in Eq.(2.43) raises the spectra at high p_T. The results in Fig. 4.6 do not fit experimental data for the entire p_T range. There are parameters such as the initial energy density that could be adjusted to match the experimental data more closely. However, in this study we could not pursue this aspect too deeply due to the substantial amount of computing time required to explore the parameter space.

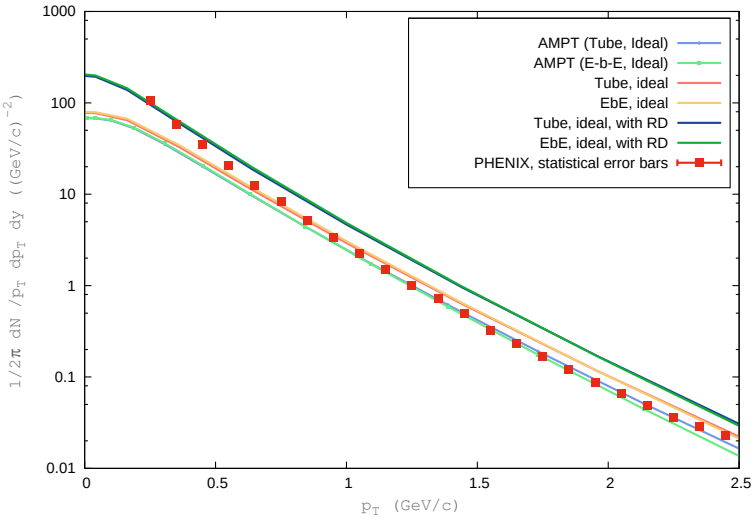

Figure 4.6: p_T-spectra for π^+ from MUSIC (with and without the inclusion of resonance decays) compared to AMPT results and PHENIX data for 30-40% centrality. Statistical error bars are too small to be seen on plot.

Fig. 4.7 show the particle spectra as a function of transverse momentum of the specified hadrons. This observable gives one an idea of the momentum distribution of particles and is measurable in experiments. The results shown in this figure are for ideal and viscous hydrodynamics and include both sets of initial conditions.

Comparing all four results from MUSIC for each particle species one sees that the initial conditions and viscosity do not change the results considerably for $p_T < 1$ GeV. After 1 GeV, the different results start to deviate. It is also interesting to note that the tube initial conditions with viscous hydrodynamics produce almost identical results of p_T-spectra to E-

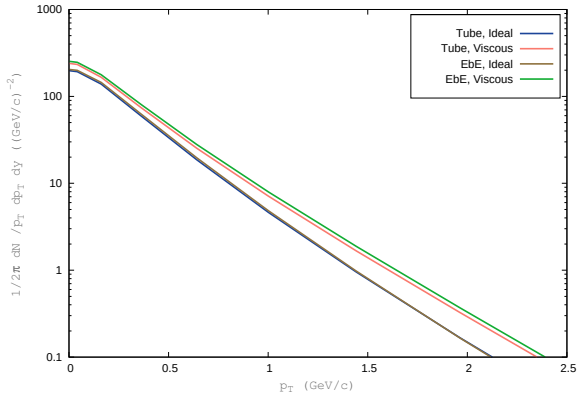

(a) π^+

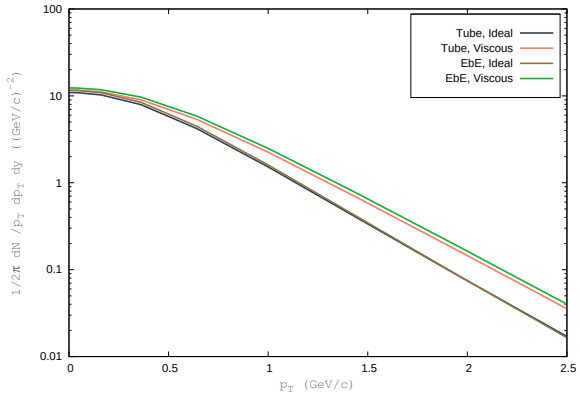

(b) K^+

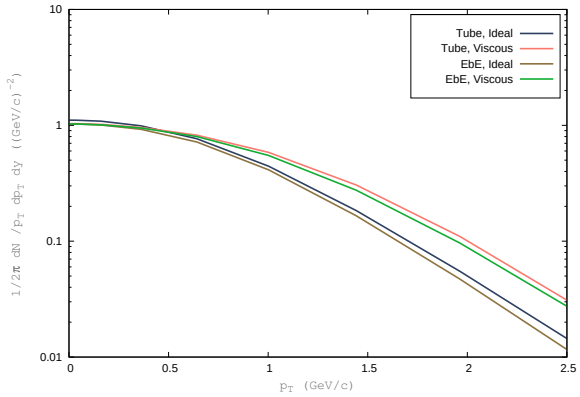

(c) p^+

Figure 4.7: p_T-spectra is shown for all computation sets for the identified hadrons. Spectra are plotted on a logarithmic scale.

by-E initial conditions with ideal hydrodynamics. Again, spectra for viscous hydrodynamics are larger than the ideal case although by a small amount. Comparing Fig. 4.7(a) to 4.7(c) shows that π particles are more likely to have higher p_T than their heavier counterparts.

4.2 Flow Coefficients

This section presents the results of flow coefficients as a function of η and p_T. The root-mean-squared (RMS) averaged flow is what should be computed in order to compare to data since this is the quantity measured in experiments. The RMS value is calculated as $\langle v_n \rangle_{\mathrm{RMS}} = \sqrt{\langle v_n^2 \rangle}$. In what follows, RMS results are quoted for flow coefficients unless stated otherwise. Fig. 4.8 shows a comparison between the average and RMS flow coefficients. Results show a 9% correction at high-p_T between $\langle v_n \rangle$ and $\langle v_n \rangle_{\mathrm{RMS}}$. Comparisons to the PHENIX data is done for charged hadrons using the event plane method [102].

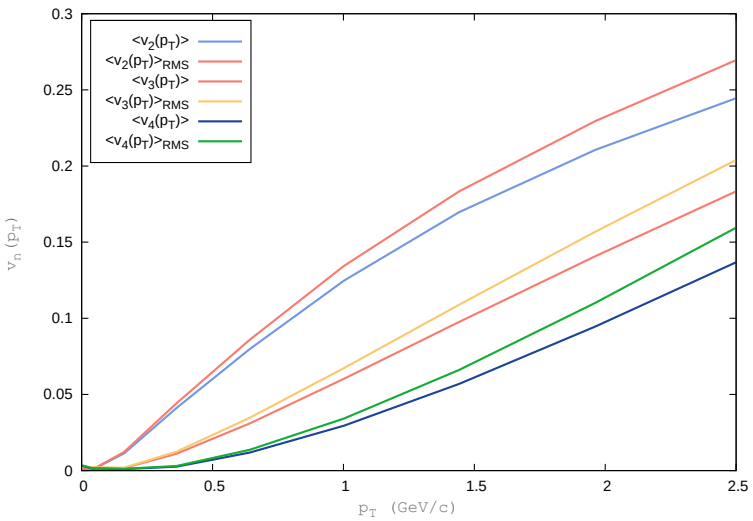

Figure 4.8: Comparing averaged and RMS flow coefficients (E-by-E ideal).

Since E-by-E initial conditions decrease the symmetry of energy density profiles, the elliptic flow coefficient v_2 is consistently lower for E-by-E compared to tube initial conditions. In order to understand this behaviour, one needs to understand the flow of the initial energy density profile. Fig. 2.2 shows that the energy density of the tube profile is flat for a certain range in η while E-by-E profiles tend to come down quickly. At near central η values,

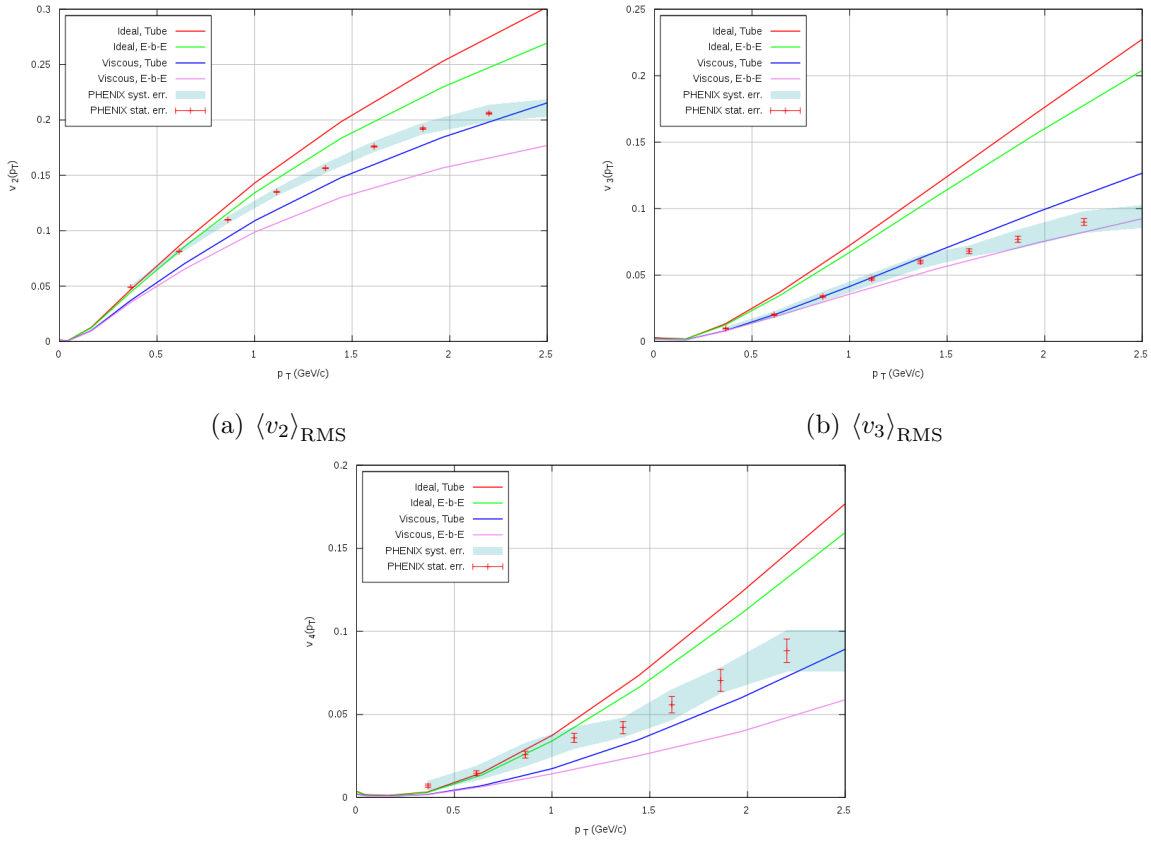

(a) $\langle v_2 \rangle_{\mathrm{RMS}}$

(b) $\langle v_3 \rangle_{\mathrm{RMS}}$

(c) $\langle v_4 \rangle_{\mathrm{RMS}}$

Figure 4.9: RMS flow plots with comparisons to PHENIX results [102]. Shaded region denotes the systematic errors and error bars indicate statistical errors.

the pressure of E-by-E events will be lower due to the quick fall down of energy density with η, while tube initial conditions will have slower flow around central η because of the energy density plateau. As a result, one can expect that the medium response to the spatial anisotropy will be smaller for E-by-E events.

In ideal hydrodynamics one expects that elliptic flow will be larger than for viscous hydrodynamics because viscosity decreases a fluid's ability to flow. This observation can be seen in Fig. 4.11. The viscous results more closely describe data and provide evidence that although QGP is almost a perfect fluid, it does contains a significant viscous component. Also, since E-by-E initial conditions decrease the symmetry of energy density profiles, the elliptic flow is consistently lower for E-by-E compared to tube initial conditions.

By definition, since the flow coefficients are related to a Fourier series expansion, Eq.(2.2),

elliptic flow is expected to be the largest type of flow. All of the flow results presented here, in particular, Figures 4.10(a) and 4.10(b) consistently show v_2 is larger than higher harmonic flow. Flow is reduced for all three flow coefficients for viscous hydrodynamics for reasons mentioned above.

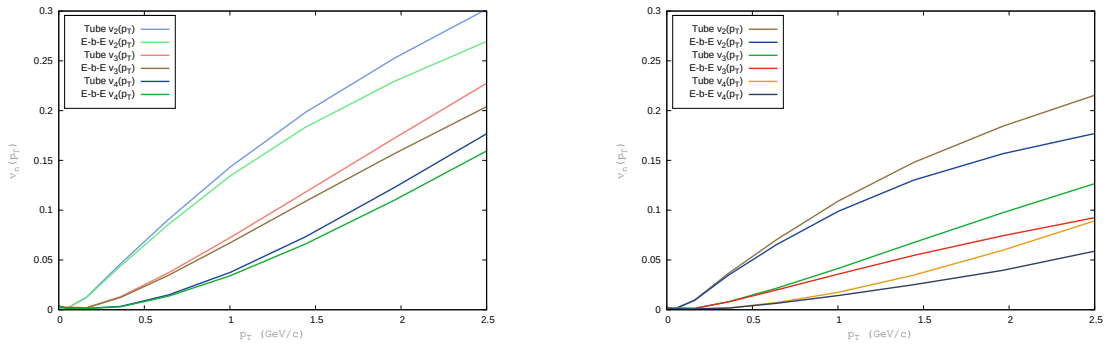

(a) Ideal evolution (b) Viscous evolution

Figure 4.10: Anisotropic flow coefficients $\langle v_n \rangle_{\mathrm{RMS}}$ as a function of transverse momentum for charged hadrons. Results are shown for both ideal and viscous hydrodynamics respectively.

One should note that at $p_T \approx 2$ GeV hydrodynamics is no longer applicable. This claim is supported by data which shows a turn over in elliptic flow at about 2 GeV after which flow decreases for larger p_T. In Fig. 4.10 one sees a slight turn over for v_2 at large p_T but this behavior is more prominent in data. One would need to put additional conditions in the hydrodynamical model to reproduce the behaviour of data at large p_T values.

Fig. 4.12 shows the results of flow coefficients as a function of η for ideal hydrodynamics with both sets of initial conditions respectively. The analysis of results for viscous hydrodynamics are similar. The results for tube initial conditions are symmetric for η and form a plateau for $|\eta| < 3$. This agrees with the initial energy profile for tube initial conditions. The E-by-E results are asymmetric but this is a statement that the sample of events was too small and fluctuations in AMPT would need a larger sample size. Results start to deviate at $\eta \approx 6$ which is a fairly large value of η to consider in hydrodynamic models.

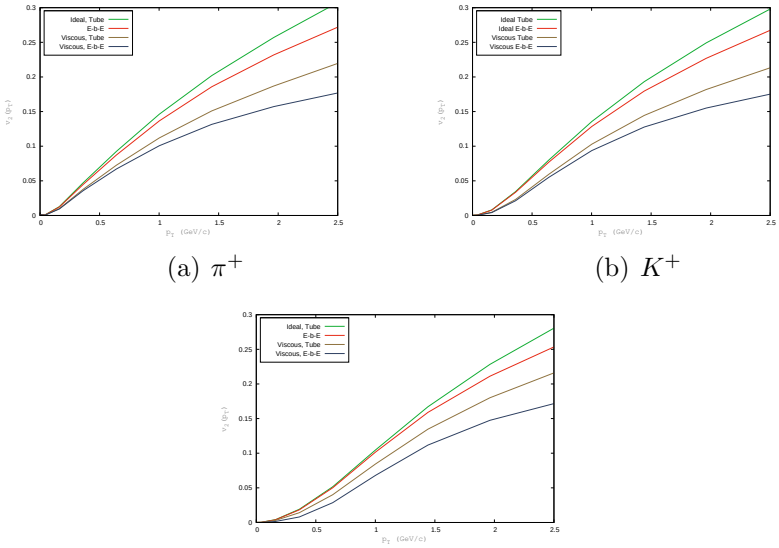

(a) π^+ (b) K^+

(c) p^+

Figure 4.11: Elliptic flow for identified charged hadrons.

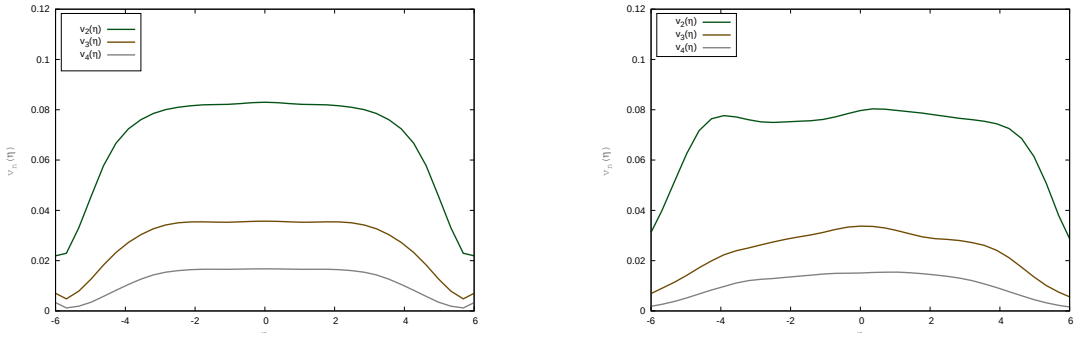

(a) Tube initial conditions (b) Fluctuating initial conditions (E-by-E)

Figure 4.12: Anisotropic flow for charged hadrons as a function of momentum pseudo-rapidity for an ideal hydrodynamic evolution and both sets of initial conditions respectively.

4.3 Mean-p_T

The results for average transverse momentum $\langle p_T \rangle$ as a function of η and y are shown for the two sets of initial conditions. These results are promising for studies like this one because the E-by-E initial conditions show the "triangular" shape seen in data, for example from the BRAHMS experiment [103]. Tube initial conditions show a flat $\langle p_T(\eta) \rangle$ instead which does not represent the shape of mean-p_T seen in data. Hence, this is one observable which can be closely compared to data to test the E-by-E initial conditions when data becomes available.

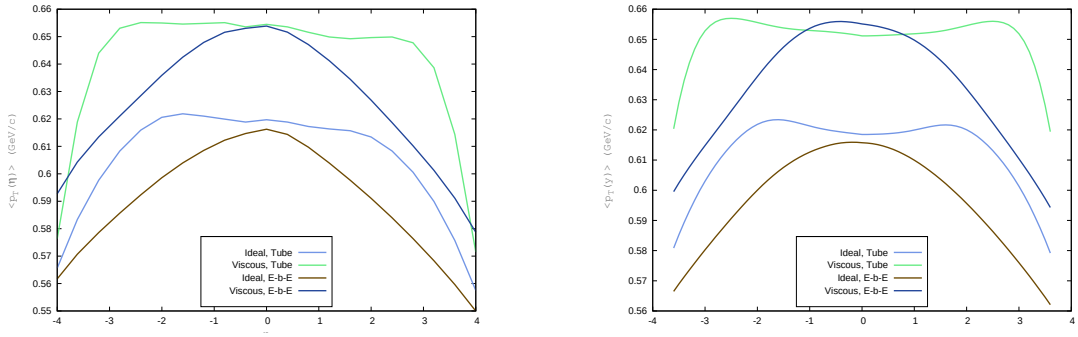

(a) $\langle p_T(\eta)\rangle$ (b) $\langle p_T(y)\rangle$

Figure 4.13: mean-p_T as a function of momentum pseudo-rapidity and dynamic-rapidity are shown for all sets of computations.

4.4 Summary of Results

In summary, the results presented in this paper agree with our physical understanding of the presented observables. Also, it is reassuring that results compare well with another group's results where they were provided. The spectra compared very well for the ideal hydrodynamic runs with both sets of initial conditions. The double-peak behaviour in spectra for E-by-E was shown to be a Jacobian effect. In tube results, this double-peak effect was always present and was believed to be a Jacobian effect. Comparing to E-by-E results confirms this speculation. The $dN/p_T dp_T dy$ calculations however, did not represent the quoted data from PHENIX. Further computations with different parameter values for initial energy density ϵ_0 could be made to fit data.

Flow coefficients in the high-p_T range computed from hydrodynamical models do not represent data. This is expected since hydrodynamics breaks down at high-p_T. The comparison of flow results to data agrees at low-p_T and could be fitted in the high-p_T range with an additional condition to the hydrodynamical model in future studies. The mean-p_T calculations show promising results from E-by-E initial conditions since they show the same triangular shape seen in data. It would be very interesting to compare these results to data once it is made available. In conclusion, these results set promising ground for further study of AMPT initial conditions in a hydrodynamical model such as MUSIC.

Chapter 5

Future Directions and Conclusion

5.1 Future Directions

There are many other studies one can conduct in the direction of initial conditions and hydrodynamical models. For one, the pair correlations as a function of $\Delta\eta$ and $\Delta\phi$ would be interesting to study with the tube and E-by-E initial conditions. It is also interesting to see what impact of the initial flow velocity will have on pair correlations since they are directly linked to flow.

Although the AMPT initial conditions captures some interesting features of data, one important missing feature in the results is the double bump feature of $dN/d\eta$ spectra for E-by-E events as a function. This feature is present in experimental data and tube initial conditions, but is not prominent in the E-by-E initial conditions. The effect is explained by a Jacobian effect, as was discussed in Fig. 4.5. Regardless of this observation, the AMPT initial conditions do capture other important behavior. Also, something which would be of great benefit to this field is the inclusion of a full initial $T^{\mu\nu}$ into the hydrodynamical simulations. The following section is devoted to this discussion.

Finally, of interest to some groups, it would be interesting to study the role of fluctuating initial conditions on electromagnetic observables. This is especially interesting because no

electromagnetic information (other than conservation of charge) is explicitly included into the initial conditions or the hydrodynamical calculation.

5.1.1 Including Complete $T^{\mu\nu}$

Including a complete initial energy-momentum tensor with ideal, shear and bulk viscosity components is also a planned endeavor for this project. The form of the complete $T^{\mu\nu}$ is as follows

$$T^{\mu\nu} = \epsilon u^{\mu} u^{\nu} + (P(\epsilon) + \Pi)\Delta^{\mu\nu} + \Pi^{\mu\nu}, \tag{5.1}$$

where, Π is the bulk viscosity and $\Pi^{\mu\nu}$ is the shear viscosity.

The initial total energy density profiles produced in AMPT are very jagged so that these peaks may eventually grow as instabilities. However, the range of energy density in the EOS (0.01 GeV to 39061 GeV) should capture all ranges possibly attainable in collisions. MUSIC is designed to treat instabilities and suppress their growth, however, the complete $T^{\mu\nu}$ was too unstable for the program. It is interesting to try to modify MUSIC to make these runs possible, however, MUSIC is the best available hydrodynamical program so other routes could be taken. First, one might be required to restrict the initial instabilities produced by AMPT by producing a more stable initial energy profile.

In order to produce a more stable energy profile, one method is to smooth out the initial conditions using the spatial median filter [104]. This is an image processing technique which can easily be borrowed for the fixed-grid hydrodynamic model. The space is divided into windows of cells around a central cell. In the simplest case, a window of 3×3 cells is used. The value of energy density in the center cell will be replaced by the median of the values of surrounding cells. This method is known for its ability to remove "impulse" noise and will make the profile increasingly smooth by removing deep drops and high peaks in local energy densities.

Above are plots of the initial shear viscosity (Fig. 5.1) as a function of one specified transverse axis and the z-axis. The viscosity should not pass unity in this scale. As can be

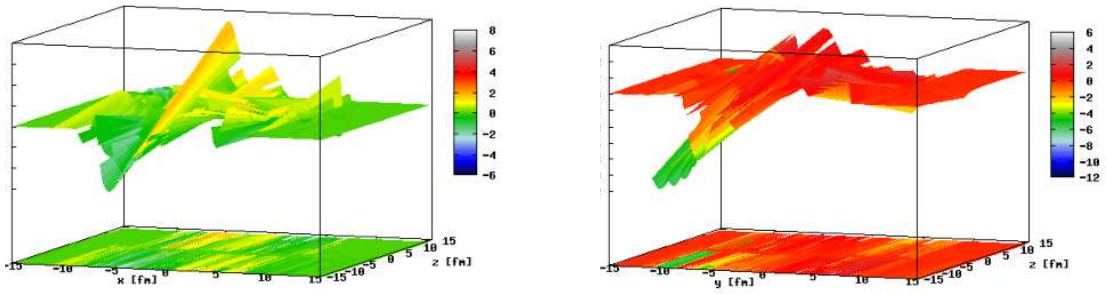

(a) W(x, z) (b) W(y, z)

Figure 5.1: Plots of shear viscosity W^{ij} for an AMPT initial condition event, at central values of η and y or x respectively. Profile is too jagged for current hydrodynamical codes.

seen in the plots, the profile exceeds unity at some points in space, and is very jagged. This profile is expected to lead to a rapid instability in the currently available hydrodynamical programs.

5.2 Conclusion

The study of relativistic hydrodynamics with fluctuating initial conditions shows promising results. The inclusion of resonance decays, shear viscosity, fluctuating initial flow velocities, and fluctuating longitudinal energy profile in simulations are important aspects of heavy-ion collisions and shows significant differences in hydrodynamical simulations. It would be of great benefit to try different parameter values such as the equation of state, initial proper-time τ_0, freeze-out temperature $T_{\rm FO}$, shear relaxation time τ_π, the inclusion of initial viscosities, and the Boltzmann viscosity correction δf to optimize results. There are also parameters in AMPT model which may be tested such as the evolution time before thermalization and cut-off time for partonic interactions. One should also repeat this study for different centrality bins.

The spectra, flow coefficients, and mean-p_T calculations were shown for tube and E-by-E initial conditions. The E-by-E results differ from tube results and provide some important new features of data such as the behaviour seen in data for $\langle p_T(\eta)\rangle$. Using a viscous hy-

drodynamical evolution was also useful in obtaining results which more closely fit data for anisotropic flow results.

In conclusion, it is clear from the results presented in this paper that the study of a hydrodynamical evolution of AMPT initial conditions guides the field in the right direction and longitudinal and initial flow fluctuations should further be tested in these models.

Appendices

Appendix A

Input Parameter Tables

Tables A.1 and A.2 show a complete list of relevant input parameters used in MUSIC and AMPT respectively. Some input parameters in these tables define theoretical and numerical parameters related to the initial conditions, others determine particle interactions and all particles species and interactions which should be considered in the simulations. Specifically, factors such as time parameters, relaxation time, viscosity, decay inclusions, freeze-out algorithm, mini-jet and nuclear effects, and grid sizes are all specified as they have been used for the results presented in this thesis.

Some input parameters here are bound to the initial conditions, such as Au+Au at $\sqrt{s_{\rm NN}} = 200$ GeV is chosen in AMPT so as to correspond to the nuclei and RHIC energy for the collision energy.

Parameter name	Parameter value [units]
EOS	2 (s95p-v1)
Do FreezeOut Yes 1, No 0	1
average freeze-out surface over	50 time steps
use energy density for freeze-out	0
T_{freeze}	0.137 GeV
Initial-profile	8
Initial Distribution Filename	file containing $T^{\mu\nu}$
freeze-out method	3
pseudofreeze	1
σ_0	0.4
output evolution data	1
η-plateau size	5.9
η fall-off	0.4
$\Delta\tau$	0.2
Minmod Theta	1.8
Runge Kutta order	2 (or 1 if unstable)
ϕ steps	10
p_T steps	10
max $\Delta\eta_2$	0.1
max η	8.0
max p_T	4.003 GeV/c
min p_T	0.00173 GeV/c
Initial τ_0	0.4 fm
Δx	0.28 fm
Δy	0.28 fm
$\Delta\eta_s$	0.3
number of particles to include	100
particle spectrum to compute	0
max y	8.
Δy	0.1
Include δf	1
Viscosity Flag	0: No, 1: Yes
Include Shear Viscosity	0: No, 1: Yes
Shear to viscosity ratio	0.08
Minimum Epsilon Frac For Visc	0.00001
Shear relaxation time τ_π	0.2 fm

Table A.1: Relevant initial condition parameters in MUSIC.

EFRM ($\sqrt{s_{\rm NN}}$ in GeV)	200
FRAME	CMS
PROJ	A
TARG	A
IAP (projectile A number)	197
IZP (projectile Z number)	79
IAT (target A number)	197
IZT (target Z number)	79
BMIN (minimum impact parameter in fm)	b_{min}
BMAX (maximum impact parameter in fm)	b_{max}
ISOFT (D=1): select Default AMPT or String Melting	4
NTMAX: number of timesteps (D=150)	3
DT: timestep in fm (hadron cascade time= DT*NTMAX) (D=0.2)	0.2
PARJ(41): parameter a in Lund symmetric splitting function	2.2
PARJ(42): parameter b in Lund symmetric splitting function	0.5
(D=1,yes;0,no) flag for popcorn mechanism(netbaryon stopping)	1
PARJ(5) to control BMBbar vs BBbar in popcorn (D=1.0)	1.0
shadowing flag (Default=1,yes; 0,no)	1
quenching flag (D=0,no; 1,yes)	0
quenching parameter -dE/dx (GeV/fm) in case quenching flag=1	1.0
p0 cutoff in HIJING for minijet productions (D=2.0)	2.0
parton screening mass in fm^{-1} (D=3.2264d0)	3.2264d0
IZPC: (D=0 forward-angle parton scatterings; 100,isotropic)	0
alpha in parton cascade	0.47140452d0
dpcoal in GeV	1d6
drcoal in fm	1d6
ihjsed: take HIJING seed from below (D=0)or at runtime(11)	11
random seed for HIJING	53153523
random seed for parton cascade	8
flag for Ks0 weak decays (D=0,no; 1,yes)	0
flag for ϕ decays at end of hadron cascade	1
optional OSCAR output (D=0,no; 1,yes; 2,initial parton info)	1

Table A.2: Relevant initial condition parameters in AMPT.

Appendix B

A Few Words on RHIC

The RHIC complex is the first experimental set-up capable of colliding heavy ions. The first set of data from RHIC was published in 2005. The center of mass energy can reach 200 GeV per nucleon pair. This is ten times the highest energy reached in previous fixed target experiments. Collisions ranging from p+p, d+Au, Cu+Cu to Au+Au have been run [47]. The simulations run by hydrodynamical programs is hence a useful tool to study the results of these experiments die to QCD medium production at the RHIC energy scale. The RHIC complex consists of two 3.8 km concentric quasi-circular superconducting storage accelerator rings. The rings share a common horizontal plane inside the tunnel, while each ring has an independent set of bending and focusing magnets and radio frequency acceleration cavities. The rings consist of 6 interaction points and 4 of these are currently used by experiments: STAR, PHENIX, PHOBOS, and BRAHMS.

Bibliography

[1] M. L. Miller, K. Reygers, S. J. Sanders, and P. Steinberg. Glauber Modeling in High-Energy Nuclear Collisions. *10.1146/annurev.nucl.57.090506.123020*, May 2007.

[2] P. Braun-Munzinger, K. Redlich, and J. Stachel. *Particle Production in Heavy Ion Collisions*. World Scientific, 2003.

[3] K. Haruna. Pseuo-Rapidity Distribution of Charged Particles in Relativistic Heavy Ion Collision. Master's thesis, Department of Physics, Graduate School of Science, Hiroshima University, Feb 2006.

[4] P. F. Kolb and U. Heinz. *Hydrodynamic Description of Ultrarelativistic Heavy-Ion Collisions*. World Scientific, 2003.

[5] Z.-W. Lin, C. M. Ko, B.-A. Li, B. Zhang, and S. Pal. A Multi-Phase Transport Model for Relativistic Heavy Ion Collisions. *Phys. Rev. C* **72, 064901**, Dec 2005.

[6] L. Pang, Q. Wang, and X.-N. Wang. Effects of Initial Flow Velocity Fluctuation in Event-by-Event (3+1)D Hydrodynamics. *Phys. Rev.* ***C86****, 024911*, Sep 2012.

[7] L. Pang, Q Wang, and X.-N. Wang. Effect of Longitudinal Fluctuation in Event-by-Event (3+1)D Hydrodynamics. *Nucl. Phys.* ***A904-905****, 811c-814c*, Nov 2012.

[8] L. Pang, Q Wang, and X.-N. Wang. Relics of Minijets Amid Anisotropic Flows in High-Energy Heavy-Ion Collisions. *Phys. Rev.* ***C89****, 064910*, Oct 2013.

[9] B. Schenke, S. Jeon, and C. Gale. 3+1D Hydrodynamic Simulation of Relativistic Heavy-Ion Collisions. *Phys. Rev.* ***C82****, 014903*, Jul 2010.

[10] B. Schenke, S. Jeon, and C. Gale. Hydrodynamic Evolution and Jet Energy Loss in Cu+Cu Collisions. *Phys. Rev.* ***C83****, 044907*, Jan 2011.

[11] B. Schenke, S. Jeon, and C. Gale. Elliptic and Triangular Flow in Event-by-Event (3+1)D Viscous Hydrodynamics. *Phys. Rev. Lett.* ***106****, 042301*, Oct 2010.

[12] C. Gale, S. Jeon, B. Schenke, P. Tribedy, and R. Venugopalan. Event-by-Event Anisotropic Flow in Heavy-Ion Collisions from Combined Yang-Mills and Viscous Fluid Dynamics. *Phys. Rev. Lett.* ***110****, 012302*, Sep 2012.

[13] B. Schenke, S. Jeon, and C. Gale. Higher Flow Harmonics from (3+1)D Event-by-Event Viscous Hydrodynamics. *Phys. Rev.* ***C85****, 024901*, Sep 2011.

[14] C. Gale, S. Jeon, B. Schenke, P. Tribedy, and R. Venugopalan. Initial State Fluctuations and Higher Harmonic Flow in Heavy-Ion Collisions. *Nucl. Phys.* ***A904-905****, 409c-412c*, Oct 2012.

[15] C. Gale, S. Jeon, and B. Schenke. Hydrodynamic Modeling of Heavy-Ion Collisions. *Int. J. Mod. Phys.* ***A28****, 1340011*, Jan 2013.

[16] J.-Y. Ollitrault. Relativistic Hydrodynamics for Heavy-Ion Collisions. *Eur. J. Phys.* ***29****, 275-302*, Jan 2008.

[17] S. Z. Belen'kji and L. D. Landau. Hydrodynamic theory of multiple production of particles. *Springer Link, Volume 3, Issue 1 Supplement, pp 15-31*, Jan 1956.

[18] P. Braun-Munzinger, J. Stachel, J. P. Wessels, and N. Xu. Thermal and Hadrochemical Equilibration in Nucleus-Nucleus Collisions at the SPS. *Phys. Lett.* ***B365****, 1-6*, Oct 1995.

[19] S. Voloshin and Y. Zhang. Flow Study in Relativistic Nuclear Collisions by Fourier Expansion of Azimuthal Particle Distributions. *Z. Phys.* ***C70****, 665-672*, Jul 1994.

[20] T. A. Trainor. Is Hydrodynamics Relevant to RHIC Collisions? *arXiv:0906.1229v1 [hep-ph]*, Jun 2009.

[21] N. Suzuki. One Dimensional Hydrodynamical Model Including Phase Transition. *Phys. Rev.* ***C81****, 044911*, Dec 2010.

[22] D. H. Rischke. Fluid Dynamics for Relativistic Nuclear Collisions. *In *Cape Town 1998, Hadrons in dense matter and hadrosynthesis* 21-70*, Sep 1998.

[23] C. Nonaka, E. Honda, and S. Muroya. (3+1)-dimensional Relativistic Hydrodynamical Expansion of Hot and Dense Matter in Ultra-Relativistic Nuclear Collision. *Eur. Phys. J.* ***C17****, 663-673*, Jul 2000.

[24] M.V. Savina, S.V. Shmatov, N.V. Slavin, and P.I. Zarubin. Global Characteristics of Nucleus-Nucleus Collisions in an Ultrarelativistic Domain. *Phys. Atom. Nucl.* ***62****, 2084-2086, Yad. Fiz.* ***62*** *2263-2265*, Jul 2000.

[25] T. Hirano. Relativistic Hydrodynamics ar RHIC and LHC. *Phys. Rev.,* ***C 65****, 011901*, 2002.

[26] K. Morita, S. Muroya, C. Nonaka, and T. Hirano. Comparison of Space-Time Evolutions of Hot/Dense Matter in $\sqrt{s_{\rm NN}} = 17$ and 130 GeV Relativistic Heavy Ion Collisions based on a Hydrodynamical Model. *Phys. Rev.* ***C66****, 054904*, Sep 2002.

[27] H. Song and U. Heinz. Causal Viscous Hydrodynamics in 2 + 1 Dimensions for Relativistic Heavy-Ion Collisions. *Phys. Rev.* ***C77****, 064901*, Jun 2008.

[28] P. F. Kolb, P. Huovinen, U. Heinz, and H. Heiselberg. Elliptic Flow at SPS and RHIC: from Kinetic Transport to Hydrodynamics. *Phys. Lett.* ***B500****, 232-240*, Dec 2000.

[29] M. Casna'd and M. Vargyas. Observables from a Solution of 1+3 Dimensional Relativistic Hydrodynamics. *Eur. Phys. J.* ***A44****, 473-478*, Sep 2011.

[30] P. Kolb. Hydrodynamic Flow at RHIC. *Heavy Ion Phys.* **15, 279**, 2002.

[31] D. A. Teaney. Viscous Hydrodynamics and the Quark Gluon Plasma. *arXiv:0905.2433v1 [nucl-th]*, May 2009.

[32] P. Romatschke. New Developments in Relativistic Viscous Hydrodynamics. *Int. J. Mod. Phys.* ***E19****, 1-53*, Oct 2009.

[33] STAR Collaboration: C. Adler *et al.* Identified particle elliptic flow in Au+Au collisions at $\sqrt{s_{\rm NN}} = 130$ GeV. *Phys. Rev. Lett.* ***87****, 182301*, Jul 2001.

[34] R. Baier, P. Romatschke, D. T. Son, A. O. Starinets, and M. A. Stephanov. Relativistic Viscous Hydrodynamics, Conformal Invariance, and Holography. *JHEP* ***0804****, 100*, Jul 2008.

[35] J.-Y. Ollitrault. Phenomenology of the Little Bang. *J. Phys. Conf. Ser.* ***312****, 012002*, Jan 2011.

[36] B. Alver and G. Roland. Collision Geometry Fluctuations and Triangular Flow in Heavy-Ion Collisions. *Phys. Rev.* ***C81****, 054905, Erratum-ibid.* ***C82****, 039903*, Jul 2010.

[37] B. H. Alver, C. Gombeaud, M. Luzum, and J.-Y. Ollitrault. Triangular Flow in Hydrodynamics and Transport Theory. *Phys. Rev.* ***C82****, 034913*, Sep 2010.

[38] Y. Schutz and U. A. Wiedemann. *Proceedings, 22nd International Conference on Ultra-Relativistic Nucleus-Nucleus Collisions.* Quark Matter 2011, Annecy, France. J. Phys. **G38**, 120301.

[39] D. V. Schroeder. *An Introduction to Thermal Physics.* Pearson Education, 2007.

[40] T. Hirano and K. Tsuda. Collective Flow and HBT Radii from a Full 3D Hydrodynamic Model with Early Chemical Freeze Out. *Nucl. Phys.* ***A715****, 821-824*, Aug 2002.

[41] C. E. Aguiar, T. Kodama, T. Osada, and Y. Hama. Smoothed Particle Hydrodynamics for Relativistic Heavy Ion Collisions. *J. Phys.* ***G27****, 75-94*, Jun 2000.

[42] C. Burgess and G. Moore. *The Standard Model: A Primer*. Cambridge University Press, 2006.

[43] J.-W. Chen, J. Deng, H. Dong, and Q. Wang. How Perfect a Gluon Plasma can be in Perturbative QCD? *Phys. Rev.* ***D83****, 034031*, Dec 2012.

[44] H. Satz. The Quark-Gluon Plasma: A Short Introduction. *Nucl. Phys.* ***A862-863****, 4-12*, Jan 2011.

[45] W. Broniowski, P. Bozek, and M. Rybczynski. Fluctuation of the Initial Condition from Glauber Models. *PoS* ***CPOD07****, 014*, Sep 2007.

[46] B. Schenke, P. Tribedy, and R. Venugopalan. Fluctuating Glasma Initial Conditions and Flow in Heavy Ion Collisions. *Phys. Rev. Lett.* ***108****, 252301*, Jun 2012.

[47] Y. Bai. *Anisotropic Flow Measurements in STAR at the Relativistic Heavy Ion Collider*. PhD thesis, University of Utrecht, Oct 2007.

[48] O. Linnyk, V. P. Konchakovski, W. Cassing, and E. L. Bratkovskaya. Photon Elliptic Flow in Relativistic Heavy-Ion Collisions: Hadronic versus Partonic Sources. *Phys. Rev.* ***C88****, 034904*, Jul 2013.

[49] C. Shen, U. Heinz, J.-F. Paquet, and C. Gale. Thermal Photons as a Quark-Gluon Plasma Thermometer Revisited. *Phys. Rev.* ***C89****, 044910*, Mar 2014.

[50] R. M. Petti. *Low Momentum Direct Photons as a Probe of Heavy Ion Collisions*. PhD thesis, Stony Brook University, Dec 2013.

[51] M. Dion, J.-F. Paquet, B. Schenke, C. Young, S. Jeon, and C. Gale. Viscous Photons in Relativistic Heavy Ion Collisions. *Phys. Rev.* ***C84****, 064901*, Nov 2011.

[52] G. Vujanovic, C. Young, B. Schenke, R. Rapp, S. Jeon, and C. Gale. Dilepton Emission in High-Energy Heavy-Ion Collisions with Viscous Hydrodynamics. *Phys. Rev.* ***C89****, 034904*, Dec 2013.

[53] P. Huovinen. Hadronic Equation of State and Relativistic Heavy Ion Collisions. In collaboration with P. Petreczky, H. Niemi and G. Denicol, Feb 2011.

[54] R. Snellings. Elliptic Flow: A Brief Review. *New J. Phys.* ***13****, 055008*, Jun 2011.

[55] U. Heinz, Z. Qiu, and C. Shen. Fluctuating Flow Angles and Anisotropic Flow Measurements. *Phys. Rev.* ***C87****, 034913*, Mar 2013.

[56] S. Jeon. Jet Quenching in Evolving QGP Medium. *Nucl. Phys.* ***A830****, 107C-114C*, Sep 2009.

[57] X.-N. Wang. Modified Fragmentation Function and Jet Quenching at RHIC. *Nucl. Phys.* ***A702****, 238*, Aug 2002.

[58] A. Donnachie and P. V. Landshoff. Soft Interactions. In *Proceedings of the Conference on New Nonperturbative Methods and Quantization of the Light Cone, Les Houches, France*, 1997.

[59] C. Young, S. Jeon, C. Gale, and B. Schenke. Monte-Carlo Simulation of Jets in Heavy-Ion Collisions. In *Proceedings of the APS Division of Particles and Fields Meeting, Providence, Rhode Island, USA*, 2011.

[60] A. Bujak *et al.* Proton-Helium Elastic Scattering from 45 to 400 GeV. *Phys. Rev.* ***D23****, 1895*, May 1981.

[61] UA5 Collaboration (G.J. Alner *et al.*). The UA5 High-Energy Anti-p p Simulation Program. *Nucl.Phys.* ***B291****, 445*, Dec 1986.

[62] J. D. Bjorken. Highly Relativistic Nucleus-Nucleus Collisions: The Central Rapidity Region. *Phys. Rev.* ***D27****, 140*, Jan 1983.

[63] P. F. Kolb, J. Sollfrank, and U. Heinz. Anisotropic Transverse Flow and the Quark-Hadron Phase Transition. *Phys. Rev.* ***C62****, 054909*, Aug 2000.

[64] P. F. Kolb, U. Heinz, P. Huovinen, K. J. Eskola, and K. Tuominen. Centrality Dependence of Multiplicity, Transverse Energy, and Elliptic Flow from Hydrodynamics. *Nucl. Phys.* ***A696****, 197-215*, May 2011.

[65] P. F. Kolb, J. Sollfrank, and U. Heinz. Anisotropic Flow from AGS to LHC Energies. *Phys. Lett.* ***B459****, 667*, 1999.

[66] W. Israel. **100**, 310. *Ann. Phys.*, 1976.

[67] J. Stewart. **A357**, 59. *Proc.Roy.Soc.Lond.*, 1977.

[68] W. Israel and J. Stewart. **118**, 341. *Ann. Phys.*, 1979.

[69] P. Huovinen. Ideal Hydrodynamics. Jet Summer School 2012, McGill University, Montreal, Canada, Jun 2012.

[70] B. Schenke. Chapter 1: How to use. Notes written for the use of MUSIC, 2010.

[71] P. D. Lax. Weak Solutions of Nonlinear Hyperbolic Equations and Their Numerical Computation. *Comm. Pure Appl. Math.*, **7**, Issue 1:159–193, Feb 1954.

[72] A. Kurganov and E. Tadmor. New High-Resolution Central Schemes for Nonlinear Conservation Laws and Convection-Diffusion Equations. *Journal of Computational Physics,* ***160****, 214*, 2000.

[73] H. Marrochio, J. Noronha, G. S. Denicol, M. Luzum, S. Jeon, and C. Gale. Solutions of Conformal Israel-Stewart Relativistic Viscous Fluid Dynamics. *arXiv:1307.6130 [nucl-th]*, Jul 2013.

[74] R. Courant, K. Friedrichs, and H. Lewy. On the Partial Difference Equations of Mathematical Physics. *IBM Jour. of Res. and Dev. Issue: 2*, 7, Mar 1967.

[75] M. Dion. Thermal Photons and Their Role in Probing the Dynamics of Heavy Ion Collisions. Master's thesis, Department of Physics, McGill University, Jun 2011.

[76] J. Noronha-Hostler, G. S. Denicol, J. Noronha, R. Andrade, and F. Grassi. Bulk and Shear Viscosity Effects in Event-by-Event Relativistic Hydrodynamics. 9th RELATIVISTIC ASPECTS OF NUCLEAR PHYSICS, 2013.

[77] K. S. Lackner. The Concept of Viscosity. Chapter 3, 2001.

[78] P. Huovinen and P. Petreczky. QCD Equation of State and Hadron Resonance Gas. *Nucl. Phys.* ***A837****, 26-53*, Dec 2009.

[79] C. Amsler *et al.* (Particle Data Group). Phys. Lett. ***B667****, 1*, 2008.

[80] U. Heinz. Concepts of Heavy-Ion Physics. In *Proceedings of the 2nd Latin American School of Conference, Sang Muguel Regla, Mexico*, 2003.

[81] K. Dusling, G. D. Moore, and D. Teaney. Radiative Energy Loss and v_2 Spectra for Viscous Hydrodynamics. *Phys. Rev.* ***C81****, 034907*, Mar 2010.

[82] R. Peschanski and E. N. Saridakis. Exact Hydrodynamic Solution for the Elliptic Flow. *Phys. Rev. C* ***80****, 024907*, 2009.

[83] P. F. Kolb and R. Rapp. Transverse Flow and Hadrochemistry in Au+Au Collisions at $\sqrt{s_{\rm NN}} = 200$ GeV. *Phys. Rev. C* ***67****, 044903*, 2003.

[84] X.-N. Wang and M. Gyulassy. HIJING: A Monte Carlo Model for Multiple Jet Production in p p, p A, and A A Collisions. *Phys. Rev.* ***D44****, 3501*, Dec 1991.

[85] B. Zhang. ZPC 1.0.1: A Parton Cascade for Ultrarelativistic Heavy Ion Collisions. *Comput. Phys. Commun.* ***109****, 193-206*, Sep 1997.

[86] J. Xu and C.M. Ko. Pb-Pb Collisions at $\sqrt{s_{\rm NN}} = 2.76$ TeV in a Multiphase Transport Model. *Phys. Rev. C* ***83****, 034904*, Mar 2011.

[87] Y. Pang and M. Gyulassy (Columbia University). OSCAR: Open Standard Codes and Routines. `https://karman.physics.purdue.edu/OSCAR`, 1997. Accessed: 2014-08-02.

[88] B. Zhang, C. M. Ko, B. A. Li, and Z. W. Lin. A Transport Model for Heavy Ion Collisions at RHIC. *Phys. Rev.* ***C72****, 064901*, Apr 1999.

[89] B. Zhang, C. M. Ko, B.-A. Li, Z. Lin, and B.-H. Sa. J/ψ Suppression in Ultrarelativistic Nuclear Collisions. *Phys. Rev.* ***C62****, 054905*, 2000.

[90] Z.-W. Lin, S. Pal, C. M. Ko, B.-A. Li, and B. Zhang. Charged Particle Rapidity Distributions at Relativistic Energies. *Phys. Rev.* ***C64****, 011902(R)*, 2001.

[91] Z.-W. Lin and C. M. Ko. Partonic Effects on the Elliptic Flow at Relativistic Heavy Ion Collisions. *Phys. Rev.* ***C65****, 034904*, 2002.

[92] Z.-W. Lin and C. M. Ko. Kaon Interferometry at RHIC from the AMPT Model. *J. Phys. Nucl. Part. Phys.* ***G30****, S263*, 2004.

[93] Z.-W. Lin, C. M. Ko, and S. Pal. Partonic Effects on Pion Interferometry at the Relativistic Heavy-Ion Collider. *Phys. Rev. Lett.* ***89****, 152301*, 2002.

[94] G. Piller, W. Ratzka, and W. Weise. Phenomenology of Nuclear Shadowing in Deep-Inelastic Scattering. *Z. Phys.* ***A352****, 427-429*, 1995.

[95] B. Badełek, K. Charchuła, M. Krawczyk, and J. Kwieciński. Small-x Physics in Deep-Inelastic Lepton-Hadron Scattering. *Rev. Mod. Phys.* ***64****, 927*, 1992.

[96] X.-N. Wang. Monte Carlo Models: *Quo Vadimus? Nucl. Phys.* ***A698****, 296-305*, May 2011.

[97] Khadija El Berhoumi. Journal Club Presentation for the Nuclear Theory Group. McGill University, 2013.

[98] C. A. Bertulani. *Nuclear Physics in a Nutshell.* Princeton University Press, 2007.

[99] K. Nakamura *et al.* (Particle Data Group). Particle Data Group. *J. Phys.* ***G37****, 075021*, 2010.

[100] H. Holopainen. *Event-by-Event Hydrodynamics and Thermal Photon Production in Ultrarelativistic Heavy Ion Collisions.* University of Jyv'askyl'a, Finland, Aug 2011.

[101] C. Loizides for the ALICE collaboration. Charged-Particle Multiplicity, Centrality and the Glauber Model at 2.76 TeV with ALICE. XII International Conference on Ultrarelativistic Nucleus-Nucleus Collisions, 2011.

[102] A. Adare *et al.* Measurements of Higher-Order Flow Harmonics in Au+Au Collisions at $\sqrt{s_{\rm NN}} = 200$ GeV. *Phys. Rev. Lett.* ***107****, 252301*, May 2011.

[103] BRAHMS Collaboration: I. G. Bearden *et al.* Charged Meson Rapidity Distributions in Central Au+Au Collisions at $\sqrt{s_{\rm NN}} = 200$ GeV. *Phys. Rev. Lett.* ***94****, 162301*, 2005.

[104] K. R. Castleman. *Digital Image Processing.* Prentice Hall, 1996.

[105] H. Niemi, K. J. Eskola, and P. V. Ruuskanen. Elliptic Flow in Nuclear Collisions at the Large Hadron Collider. *Phys. Rev.* ***C79****, 024903*, Jun 2008.

[106] A. Enokizono. *Space-Time Evolution of Hot and Dense Matter Probed by Bose-Einstein Correlation in Au+Au Collisions at* $\sqrt{s_{\rm NN}} = 200$ *GeV.* PhD thesis, Graduate School of Science, Hiroshima University, Sep 2004.

[107] S. A. Voloshin, A. M. Poskanzer, and R. Snellings. Collective Phenomena in Non-Central Nuclear Collisions. *arXiv:0809.2949v2*, Oct 2008. Draft.

[108] A. M. Poskanzer and S. A. Voloshin. Methods for Analyzing Anisotropic Flow in Relativistic Nuclear Collisions. *Phys. Rev.* ***C58****, 1671-1678*, Jun 1998.

[109] J.-Y. Ollitrault. Flow Systematics from SIS to SPS Energies. *Nucl. Phys.* ***A638****, 195-206*, Feb 1998.

[110] M. Luzum and J.-Y. Ollitrault. Directed Flow at Midrapidity in Heavy-Ion Collisions. *Phys. Rev. Lett.* ***106****, 102301*, Mar 2011.

[111] M. Bleicher, K. A. Bugaev, P. Rau, A. S. Sorin, J. Steinheimer, and H. Stöker. Directed Flow at Midrapidity in Heavy-Ion Collisions. *Phys. Rev. Lett.* ***106****, 102301*, Mar 2011.

[112] E. Richardson. Latest Flow Results from PHENIX at RHIC. *PoS* ***QNP2012****, 146*, Jun 2012.

[113] T.J. Hallman, D.E. Kharzeev, J.T. Mitchell, and T.S. Ullrich. *Proceedings of the 15th International Conference on Ultrarelativistic Nucleus-Nucleus Collisions (QM 2001).* Quark Matter 2001, Stony Brook, New York. Nucl. Phys. **A698**, 1.

[114] H. Gutbrod, J. Aichelin, and K. Werner. *Proceedings of the 16th International Conference on Ultrarelativistic Nucleus-Nucleus Collisions (QM 2002).* Quark Matter 2002, Nantes, France. Nucl. Phys. **A715**, 1.

[115] R. Snellings. Anisotropic Flow. Trento, Italy, 2004.

[116] C. Nonaka and S. A. Bass. Space-Time Evolution of Bulk QCD Matter. *Phys. Rev.* ***C75****, 014902*, Jul 2006.

[117] A. Muronga. Relativistic Dynamics of Non-Ideal Fluids: Viscous and Heat-Conducting Fluids I. General Aspects and 3+1 Formulation for nuclear Collisions. *Phys. Rev.* ***C76****, 014909*, Jul 2007.

[118] T. Hirano. Is Early Thermalization Achieved only near Midrapidity at RHIC? *Phys. Rev.* ***C65****, 011901*, Aug 2001.

[119] J. Noronha-Hostler, G. S. Denicol, J. Noronha, R. P. G. Andrade, and F. Grassi. Bulk and Shear Viscosity Effects in Event-by-Event Relativistic Hydrodynamics. *Phys. Rev.* ***C88****, 044916*, May 2013.

[120] P. Braun-Munzinger, J. Stachel, J. P. Wessels, and N. Xu. Thermal Equilibration and Expansion in Nucleus-Nucleus Collisions at the AGS. *Phys. Lett.* ***B344****, 43-48*, Nov 1994.

[121] U. Heinz and R. Snellings. Collective Flow and Viscosity in Relativistic Heavy-Ion Collisions. *Ann. Rev. Nucl. Part. Sci.* ***63****, 123-151*, Jan 2013.

[122] X.-N. Wang W.-T. Deng. Multiple Parton Scattering in Nuclei: Modified DGLAP Evolution for Fragmentation Functions. *Phys. Rev.* ***C81****, 024902*, Mar 2010.

[123] S. Pratt and . Schindel. Is HBT really puzzling? *AIP Conf. Proc.* ***828****, 430-435*, Nov 2006.

[124] STAR Collaboration: K. H. Ackermann *et al.* Elliptic Flow in Au+Au Collisions at $\sqrt{s_{\rm NN}} = 130$ GeV. *Phys. Rev. Lett.* ***86****, 402-407*, Sep 2000.

[125] J.-Y. Ollitrault. Anisotropy as a Signature of Transverse Collective Flow. *Phys. Rev.* ***D46****, 229*, Jul 1992.

[126] STAR Collaboration. Azimuthal Anisotropy in Au+Au Collisions at $\sqrt{s_{\rm NN}} = 200$ GeV. *Phys. Rev.* ***C72****, 014904*, May 2005.

[127] PHENIX Collaboration: A. Afanasiev *et al.* Systematic Studies of Elliptic Flow Measurements in Au+Au Collisions at $\sqrt{s_{\rm NN}} = 200$ GeV. *Phys. Rev.* ***C80****, 024909*, May 2009.

[128] Phobos Collaboration. Centrality and Pseudorapidity Dependence of Elliptic Flow for Charged Hadrons in Au+Au Collisions at $\sqrt{s_{\rm NN}} = 200$ GeV. *Phys. Rev.* ***C72****, 051901*, Dec 2005.

[129] J. Jia for the ATLAS Collaboration. Measurement of Elliptic and Higher Order Flow from ATLAS Experiment at the LHC. *J. Phys.* ***G38*** *124012*, Jul 2011.

[130] Y. Hama, T. Kodama, and O. Socolowski Jr. Topics on Hydrodynamic Model of Nucleus-Nucleus Collisions. *Braz. J. Phys. vol. 35 no. 1 São Paulo*, Mar 2005.

[131] P. Huovinen, P.F. Kolb, U. Heinz, P.V. Ruuskanen, and S. Voloshin. Radial and Elliptic Flow at RHIC: Further Predictions. *Phys. Lett.* ***B503****, 58-64*, Jan 2001.

[132] U. W. Heinz and P. F. Kolb. Early Thermalization at RHIC. *Nucl. Phys.* ***A702****, 269-280*, Nov 2001.

[133] H. Satz. Quark Matter and Nuclear Collisions: A Brief History of Strong Interaction Thermodynamics. *Int. J. Mod. Phys.* ***E21****, 1230006*, Jul 2012.

[134] Z.-W. Lin, S. Pal, C. M. Ko, B.-A. Li, and Bin Zhang. Multiphase Transport Model for Heavy Ion Collisions at RHIC. *Nucl. Phys.* ***A698****, 375-378*, May 2001.

[135] S. Eremin and S. Voloshin. Nucleon Participants or Quark Participants? *Phys. Rev.* ***C67****, 064905*, May 2003.

[136] J.-W. Chen, Y.-F. Liu, Y.-K. Song, and Q. Wang. Shear and Bulk Viscosities of a Weakly Coupled Quark Gluon Plasma with Finite Chemical Potential and Temperature—Leading-Log Results. *Phys. Rev.* ***D87****, 3, 036002*, Dec 2012.

[137] B. Schenke, S. Jeon, and C. Gale. Anisotropic Flow in $\sqrt{s_{\rm NN}}$ = 2.76 tev Pb+Pb Collisions at the LHC. *Phys. Lett.* ***B702****, 59-63*, Jun 2011.

[138] Md. Rihan Haque, Md. Nasim, and B. Mohanty. Elliptic and Triangular Flow in Asymmetric Heavy-Ion Collisions. *Phys. Rev.* ***C84****, 067901*, Nov 2011.

[139] S. Pal and M. Bleicher. Medium Information from Anisotropic Flow and Jet Quenching in Relativistic Heavy Ion Collisions. *J. Phys. Conf. Ser.* ***420****, 012027*, Sep 2012.

[140] L. Xu, L. Yi, D. Kikola, J. Konzer, F. Wang, and W. Xie. Model Independent Decomposition of Flow and Nonflow in Relativistic Heavy-Ion Collisions. *Phys. Rev.* ***C86****, 024910*, Oct 2012.

[141] C.-H. Chen. *Search for Jet Interactions with Quark-Gluon Plasma.* PhD thesis, Stony Brook University, Aus 2011.

[142] A. Accardi, F. Arleo, W.K. Brooks, D. D'Enterria, and V. Muccifora. Parton Propagation and Fragmentation in QCD Matter. *Riv. Nuovo Cim.* ***32****, 439-553*, Jul 2009.

[143] J. Beringer *et al.* (Particle Data Group). Review of Particle Physics. *Phys. Rev. D* ***86****, 010001*, Jul 2012.

[144] STAR Collaboration: B.I. Abelev *et. al.* Systematic Measurements of Identified Particle Spectra in pp, d+Au and Au+Au Collisions from STAR. *Phys. Rev.* ***C79****, 034909*, Apr 2009.

[145] H. van Hecke (for the PHENIX Collaboration). Measuring Charm and Bottom using the PHENIX Silicon Vertex Detectors. *PHENIX Publications, Quark Matter Proceedings 2008*, May 2008.

[146] B. B. Back *et al.* (PHOBOS collaboration). The Significance of the Fragmentation Region in Ultrarelativistic Heavy Ion Collisions. *Phys. Rev. Lett.* ***91****, 052303*, Jun 2003.

[147] PHENIX Collaboration: S. S. Adler *et al.* Identified Charged Particle Spectra and Yields in Au+Au Collisions at $\sqrt{s_{\mathrm{NN}}} = 200$ GeV. *Phys. Rev.* ***C69****, 034909*, Jul 2003.

[148] K. M. Walsh. The Glue That Binds Us All. *Brookhaven National Laboratory: News*, Jun 2012.

[149] CMS Collaboration. Observation of Long-Range Near-Side Angular Correlations in Proton-Proton Collisions at the LHC. *JHEP* ***1009****, 091*, Sep 2010.

[150] D. Velicanu for the CMS collaboration. Ridge Correlation Structure in High Multiplicity pp Collisions with CMS. *J. Phys.* ***G38****, 124051*, Jul 2011.